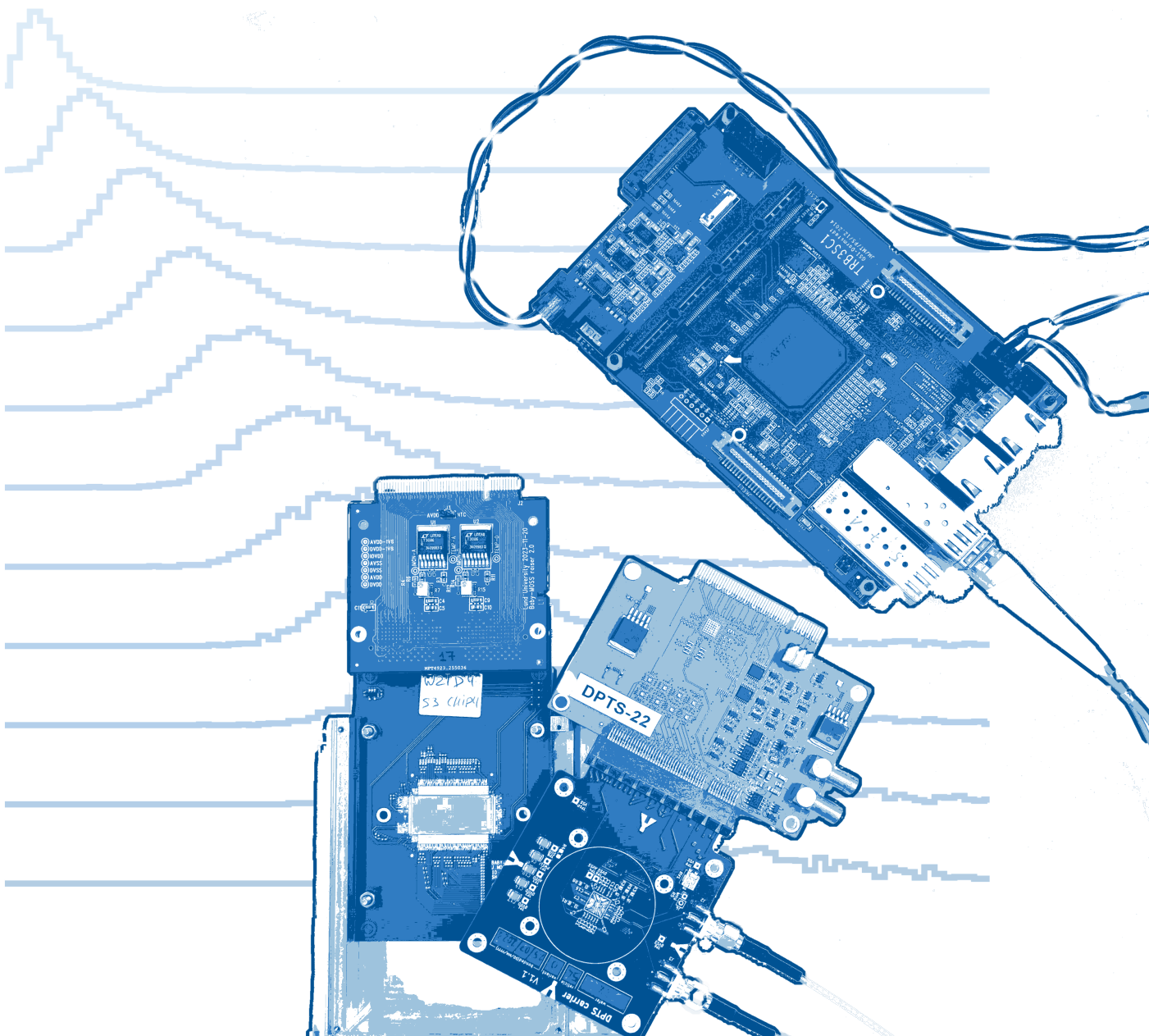
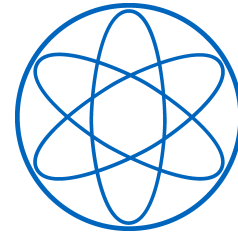


Master's Thesis

# Exploring Amplitude Measurements with MAPS Detectors

Henrik Fribert





# Exploring Amplitude Measurements with MAPS Detectors

## Erforschung von Amplitudenmessungen mit MAPS Detektoren

Dense and Strange Hadronic Matter E62

Master's Thesis

**Author:** Henrik Fribert

**Primary Reviewer:** Prof. Dr. Laura Fabbietti

**Supervisor:** Berkin Ulukutlu

**Date:** 11.10.2024

# Disclaimer

I confirm that the results presented in this master's thesis are my own work, and I have documented all sources and materials used.

Ich versichere hiermit, dass ich die von mir eingereichte Masterarbeit selbstständig verfasst und keine anderen als die angegebenen Quellen und Hilfsmittel benutzt habe.

Munich, 11.10.2024

A handwritten signature in blue ink that reads "Henning Fröding". The signature is written in a cursive style with a large, sweeping flourish at the end.

---

Place, Date

Signature

# Abstract

Monolithic Active Pixel Sensors (MAPS) are a tracking detector technology that is expected to be highly important for future experiments due to their rapid integrability. The ALICE experiment is at the forefront of the R&D of MAPS detectors with the ITS2 and currently ongoing ITS3 project.

This thesis provides a detailed investigation into amplitude measurements using MAPS detectors, utilizing prototype sensors developed in the scope of the ITS3 project. The ability of amplitude measurement would have an immense impact on the performance of MAPS trackers of the future. One way of implementing this is based on the Time-over-Threshold (ToT) method. To demonstrate its feasibility, studies were conducted with the DPTS and BabyMOSS sensors, along with simulations.

Utilizing the DPTS, an FPGA-based readout was implemented using a TRB3 board with TDC-in-FPGA technology. This setup is capable of decoding the time-encoded hit position and Time-over-Threshold (ToT) information, making it suitable for large-scale experiments. The performance of this readout was evaluated and found to be almost equivalent to the existing picoscope readout method. This result paves the way for next-generation detectors that employ technology similar to the DPTS.

In the work with the BabyMOSS sensor, successful demonstrations of ToT measurements were achieved using the digital oversampling method, both with a radioactive source and in a test beam environment. This approach not only confirmed the feasibility of ToT measurements but also allowed for extrapolation towards a multi-layer detector system. Findings indicate that such a system could significantly enhance energy resolution. To support these studies, Geant4 simulations were conducted involving multiple silicon layers, investigating the energy deposition of various particles at different momenta. These simulations explored the effects of key parameters, including the sampling period, analog signal length, and sensor thickness, on the separation power. Results suggest that with optimized parameters, sufficient separation of pions and protons can be achieved up to  $0.7 \text{ GeV}/c$ .

These findings are particularly relevant for future experiments with integrated MAPS detectors, such as the planned ALICE3 project, which could greatly benefit from enhanced particle identification and additional amplitude information.

# Contents

<b>1</b>	<b>Introduction</b>	<b>1</b>
1.1	Particle Tracking Detectors . . . . .	1
1.2	ALICE . . . . .	2
1.3	MAPS . . . . .	4
1.4	ITS3 Upgrade . . . . .	5
1.4.1	DPTS . . . . .	6
1.4.2	BabyMOSS . . . . .	8
<b>2</b>	<b>Implementing an FPGA-Based Readout for Direct ToT-Measurement</b>	<b>11</b>
2.1	DPTS Working Principle . . . . .	11
2.1.1	Decoding . . . . .	11
2.1.2	ToT and Fake-Hit Rate . . . . .	15
2.1.3	Energy Spectrum . . . . .	16
2.2	FPGA-Readout TDC Implementation for Decoding . . . . .	18
2.3	Performance . . . . .	22
<b>3</b>	<b>ToT-Measurement with Digital Oversampling</b>	<b>29</b>
3.1	Oversampling Method . . . . .	29
3.2	Tests with BabyMOSS . . . . .	32
3.2.1	Source Measurements . . . . .	32
3.2.2	Test Beam Measurements . . . . .	38
<b>4</b>	<b>Impact and Feasibility of Amplitude Measurement for Pixel Detectors</b>	<b>48</b>
4.1	State-of-the-Art PID . . . . .	48
4.2	Example Use-Case for the ALICE3 Outer Tracker . . . . .	50
4.3	Geant4 Simulation . . . . .	51
<b>5</b>	<b>Conclusion and Outlook</b>	<b>57</b>
	<b>Appendix</b>	<b>60</b>
	<b>List of Figures</b>	<b>64</b>
	<b>List of Tables</b>	<b>68</b>
	<b>Bibliography</b>	<b>69</b>

# 1 Introduction

## 1.1 Particle Tracking Detectors

Particle detectors are essential tools in modern physics experiments, enabling scientists to study the fundamental properties of matter and the underlying forces of nature. One of the hot spots for studying these properties is the Large Hadron Collider (LHC) at CERN [1] in Geneva. At the accelerator complex, ultra-relativistic protons and heavy ions collide, producing up to thousands of particles per collision that are measured to gain insights into the physics. However, many of the primary particles produced in these collisions are short-lived and decay before being measured, creating secondary vertices some distance away from the original interaction point. To accurately reconstruct these particles and, in general, understand the underlying processes with high precision, one needs a dedicated detector system that can precisely measure the trajectories and properties of the particles. A simple example of what a detector system could incorporate is a tracking detector, calorimeters to obtain information on the energy, as well as detectors for particle identification (PID) such as Time-of-Flight (TOF) [2] or Ring Imaging Cherenkov (RICH) [3] detectors. This thesis will focus specifically on tracking detectors and the possibility of obtaining information on the energy of the particles.

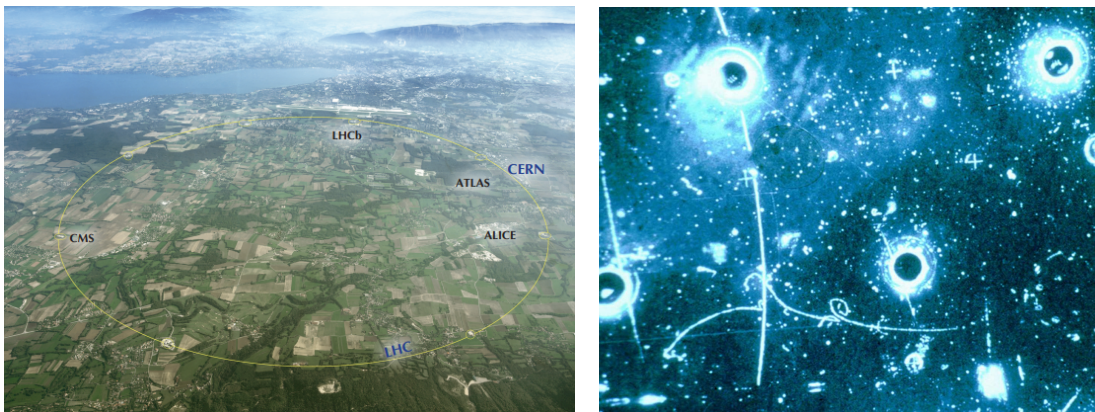


Figure 1.1: Left: Aerial view of the LHC accelerator complex at CERN in Geneva, Switzerland [4]. Right: A picture of the tracks that were captured using a bubble chamber, which led to the discovery of the Z boson and the associated evidence for the weak neutral current [5].

## 1 Introduction

Particle trackers come in various forms, including older technologies developed in the early to mid-20th century, such as bubble chambers [6] and cloud chambers [7], in which the tracks were made visible and recorded with a camera, leading to significant discoveries like the Z-boson. Later pioneering tracking detectors included Multi-Wire Proportional Chambers (MWPCs) [8], which can be used to construct Time-Projection Chambers (TPCs) that are capable of producing a 3-dimensional reconstruction of the particle tracks. However, in the last decades and years, a focus has been laid on using silicon devices for particle tracking purposes, such as silicon strip or pixel detectors [9]. Silicon trackers [10, 11] can have several advantages over other technologies, such as high spatial resolution, fast response time, low material budget, etc.

### 1.2 ALICE

The ALICE experiment (A Large Ion Collider Experiment) [12] is one of the four major detectors at the LHC, positioned at Interaction Point 2. Its primary objective is to explore the properties of Quantum Chromodynamics (QCD) [13], which describes the fundamental strong interaction between particles such as gluons and quarks, which make up the hadronic matter such as protons, neutrons, or pions.

A central focus of ALICE is the study of the Quark-Gluon Plasma (QGP) [14], a deconfined phase of quarks and gluons that is believed to have existed in the early universe several microseconds after the Big Bang. Under extreme conditions of temperature and energy density, such as those achieved in ultra-relativistic heavy-ion collisions (e.g., Pb-Pb collisions), quarks and gluons are no longer confined within hadrons but form a strongly interacting, nearly perfect fluid. The ALICE detector is designed to study the properties and dynamics of this QGP state by examining a broad range of collision products, including hadrons, photons, leptons, and heavy-flavor quarks.

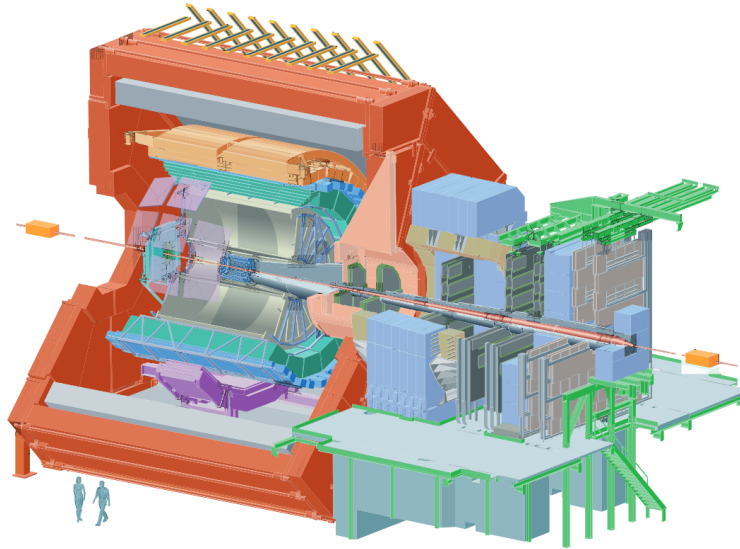


Figure 1.2: A schematic layout of the ALICE experiment and the present subdetectors. [12]

The ALICE experiment relies on a highly sophisticated and specialized detector system to achieve its physics goals and extract valuable data from collisions. This complex system, illustrated in Figure 1.2, consists of several subdetectors, each designed to perform specific tasks such as particle tracking, identification, and energy measurement. Central to the tracking capabilities of ALICE are the Inner Tracking System (ITS) [15] and the Time Projection Chamber (TPC) [16], which work together to provide a precise reconstruction of particle trajectories.

The TPC is a large, gas-filled chamber that utilizes Gas Electron Multiplier (GEM) detectors [17]. These detectors enable the TPC not only to precisely track charged particles but also to perform particle identification (PID) by measuring the specific energy loss ( $dE/dx$ ) as particles traverse the gas. As charged particles move through the gas, they ionize the gas molecules along their path. The energy loss depends on the particle's velocity and charge, making it a key observable for distinguishing between various particle species. For instance, lighter particles such as pions will lose less energy compared to heavier particles like protons at similar momenta. This difference in energy loss allows the TPC to effectively separate different particle types, such as pions, kaons, and protons.

The Inner Tracking System (ITS), located closest to the collision point, is based on silicon detector technology. During the Long Shutdown 2 (LS2), the original ITS was upgraded and replaced with an advanced silicon tracker based on Monolithic Active Pixel Sensor (MAPS) technology. This new ITS enhances tracking precision and spatial resolution, allowing ALICE to detect particles with much greater accuracy, particularly at low momenta.

### 1.3 MAPS

Monolithic Active Pixel Sensors (MAPS) [18, 19] are advanced detectors that integrate the sensing diodes and the readout circuitry into the same pixel, distinguishing them from hybrid pixel detectors, where these components are separate and interconnected via methods like bump bonding. The working principle of MAPS is analogous to that of other silicon detectors and is fundamentally based on the generation of electron-hole pairs in the depletion region, followed by the collection of charge on the collection diode.

When an ionizing particle passes through the detector volume, it interacts with the silicon lattice, creating electron-hole pairs. The electrons diffuse through the material until they either reach the depletion region or are generated directly within it. The depletion region, represented in white in Figure 1.3, is characterized by an electric field generated by the bias voltage applied across the detector. This electric field causes the electrons to drift toward the collection diode while the positively charged holes move in the opposite direction.

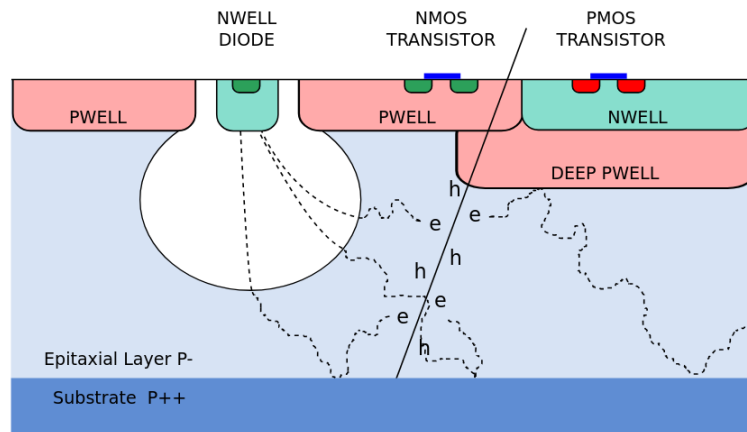


Figure 1.3: Working principle and schematic cross-section of a MAPS pixel. [20]

This charge movement induces an electric signal in the readout circuitry, which is then processed and transmitted as an output. The efficiency of charge collection and the collection time can be influenced by factors such as the thickness of the sensor, the applied bias voltage, and the doping profile of the pixels. In general, silicon sensors are favored in particle detection due to their excellent charge collection efficiency, high spatial resolution, and precise energy resolution.

MAPS detectors, in particular, offer several advantages over alternative technologies. In addition to their overall high resolution and accuracy, MAPS can be mass-produced at relatively low costs, making them accessible for large-scale experiments. Their monolithic structure results in a lower material budget com-

pared to hybrid sensors, which is essential for minimizing multiple scattering effects and optimizing track resolution in high-energy physics environments.

## 1.4 ITS3 Upgrade

The current Inner Tracking System (ITS2) of the ALICE experiment is composed of seven silicon detector layers, arranged into the Inner Barrel (IB) containing layers 0-2 and the Outer Barrel (OB) comprising layers 3-6. These layers are made up of staves, each equipped with monolithic active pixel sensors known as ALPIDE chips [21, 22], specifically developed for ITS2. These sensors were fabricated using the TowerJazz 180 nm CMOS Imaging Process.

As part of an ALICE upgrade plan, the ITS3 [23, 24] will be implemented during Long Shutdown 3 (LS3). The three innermost layers of the current ITS2 will be replaced with a new generation of MAPS detectors that utilize the more advanced 65 nm CMOS technology. Importantly, the traditional stave-based structure will be replaced with two lightweight, ultra-thin half-barrels, each containing three layers. This redesign aims to drastically reduce the material budget, which is crucial for minimizing multiple scattering effects and improving track resolution, particularly for low-momentum particles.

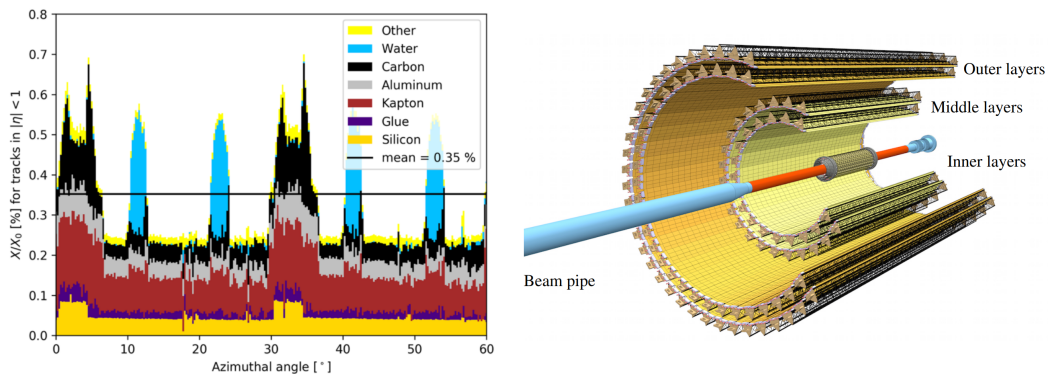


Figure 1.4: Left: The various contributions to the material budget with the current ITS2 geometry [20]. Right: A schematic of the outer and the inner barrel of the ITS2 in the stave configuration [23].

Several improvements will be implemented to achieve the material budget reduction in the ITS3 upgrade. A significant advance is the introduction of a truly cylindrical detector design, which enables the removal of most traditional support structures such as staves and cooling pipes. This new design will rely almost entirely on active detection material. The silicon wafers that form the tracking layers will be stitched sensors that are bent into a cylindrical shape, eliminating the need for bulky support infrastructure.

## 1 Introduction

To ensure the proper positioning of the layers, carbon foam as a lightweight spacer will be used, minimizing material usage while maintaining the correct geometry. These reductions in the material are crucial for decreasing multiple scattering and improving both vertex resolution and tracking accuracy, especially for low transverse momentum ( $p_T$ ) particles. Additionally, the current beam pipe will be replaced with a thinner version and positioned closer to the interaction point, which will reduce the material budget even further. To develop the new tracking system, the community created and tested several prototypes incorporating the new technology. These prototypes include the APTS [25], DPTS [26], CE-65 [27], BabyMOSS, and MOSS [28]. In this thesis, two of these prototypes, the DPTS and the BabyMOSS, were investigated.

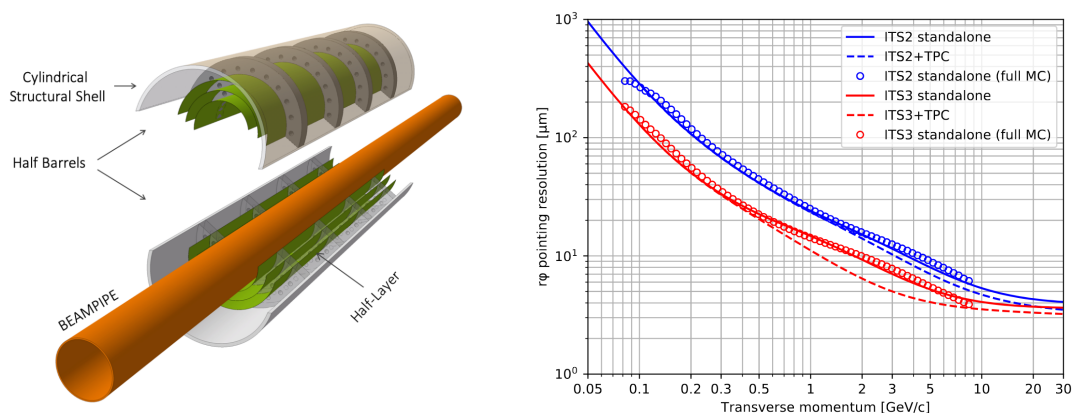


Figure 1.5: Left: A schematic of the two ITS3 half barrels with cylindrical geometry supported by carbon foam. Right: The pointing resolution of the ITS2 in comparison to the expected performance of the ITS3 upgrade as a function of the transverse momentum [23].

### 1.4.1 DPTS

The Digital Pixel Test Structure (DPTS) is a small prototype with  $32 \times 32$  rows and columns, amounting to a total of 1024 pixels with a pitch of  $15 \times 15 \mu\text{m}^2$ . It was developed together with the Analog Pixel Test Structure (APTS) as part of Engineering Run 1 (ER1) to test the digital front-end of the technology, whereas the APTS was used to analyze the analog response of chips. All the pixels are read out simultaneously via a differential digital output line, and the pixel position is time encoded. Additionally, it is possible to extract the analog output of one of the pixels using the monitoring pixel (31, 31). The DPTS was designed in such a way that information on the injected or measured charge in the pixel can be obtained by measuring the Timer-over-Threshold (ToT). The exact working principle will be explained later in detail in chapter 2.

# 1 Introduction

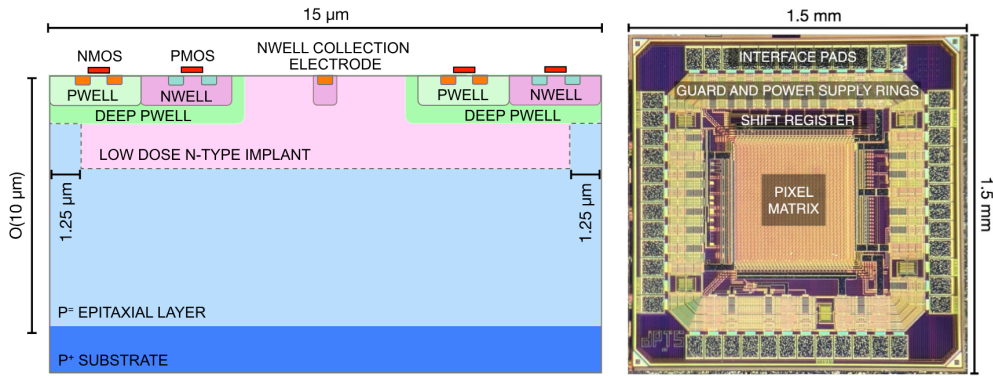


Figure 1.6: The pixel cross-section of the modified with gap process and a photo of the DPTS under a microscope [26].

Shown in Figure 1.6 is, next to a photo of the DPTS, the cross-section of the pixels that will be used for the ITS3. Additionally to the MAPS design discussed previously, the pixel incorporates a low-dose n-type implant in the epitaxial layer. This modification was made to extend the volume of the depletion region to cover almost the full pixel width of 10 μm and, therefore, accelerate and collect more charges. Gaps without this additional implant were introduced at the border of the pixels to increase the electric field in the lateral direction, thereby increasing the collection time of charges generated close to the pixel border and decreasing charge-sharing amidst neighboring pixels.

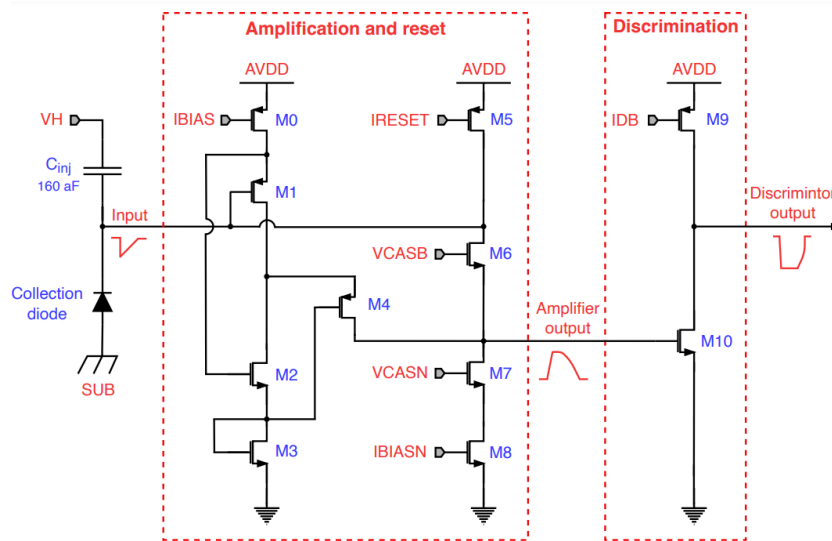


Figure 1.7: DPTS in-pixel front end, used for amplification, reset, and discrimination. [26]

The diagram in Figure 1.7 shows the analog front-end circuit of the DPTS. It includes an amplification and discrimination stage made up of several transis-

tors. The circuit can be controlled using two voltages - VCASN and VCASB, and four currents - IBIAS, IBIASN, IDB, and IRESET. These parameters can be adjusted to set the threshold of the pixels via VCASN and VCASB or to adjust the threshold of the second stage (discrimination) via IDB. Additionally, the length of the analog signal can be changed using IRESET, which is responsible for resetting the pixel by providing a constant current and also ensures a proportional charge-to-ToT behavior. To pulse the pixels individually, a capacitor with 160 pF was implemented, through which a charge can be injected into the collection diode by applying an external voltage.

### 1.4.2 BabyMOSS

In order to test the new stitching technology for the wafer scale sensors, another prototype was built, with which one can investigate not only the stitching techniques and the yield but also the power distribution and data transmission along a large detector. Therefore, this prototype was named MOSS, which stands for MOnolithic Stitched Sensor [28, 29]. The MOSS consists of smaller segments called Repeating Sensor Units (RSUs) that are connected together through the stitching technique, which makes it possible to create sensors with a much larger active area than the RSU itself. The principle of stitching is illustrated in Figure 1.8, where it can be seen how reticles are combined to create one larger sensor.

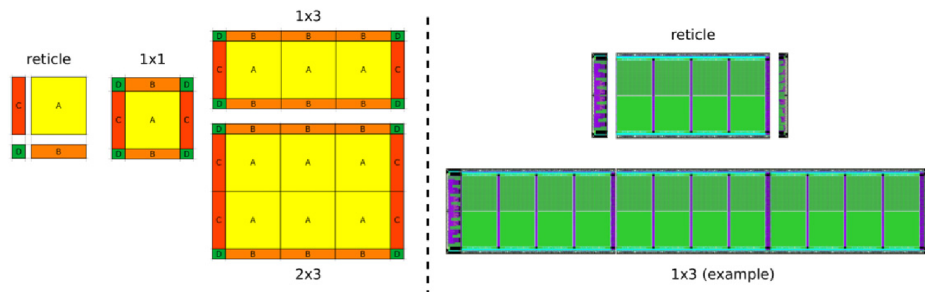


Figure 1.8: An example of how reticles are combined to form single sensors of a larger scale and active area. [28]

The MOSS itself consists of ten RSUs stitched together in one direction to form one long sensor with a length of 25.9 cm. Each RSU is divided into a top and a bottom half-unit, as shown in Figure 1.9.

## 1 Introduction

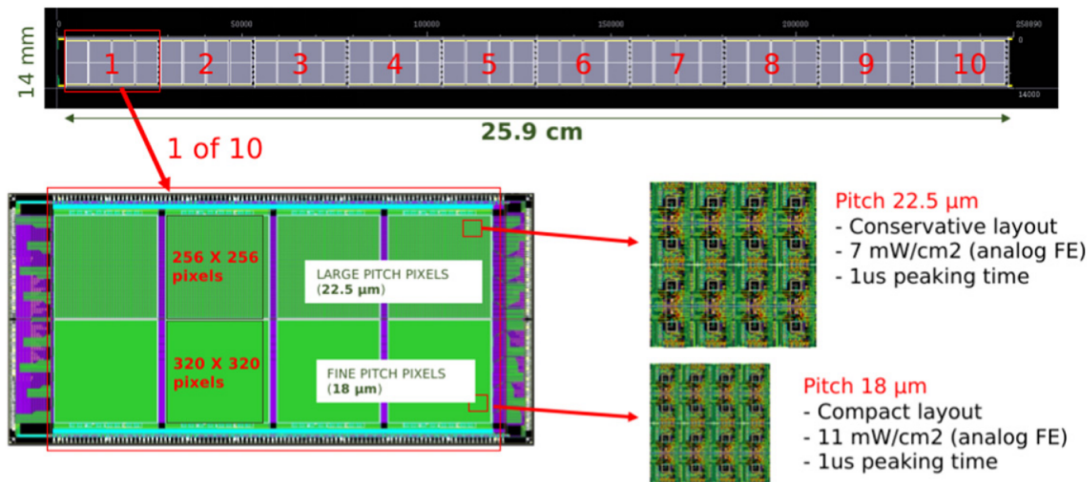


Figure 1.9: The MOSS detector with ten stitched RSUs, which are each divided into top and bottom half-units with four different regions. [28]

The top unit consists of pixels with a pitch of  $22.5 \times 22.5 \mu\text{m}^2$ , whereas the bottom half has a pixel size of  $18 \times 18 \mu\text{m}^2$ . Each half-unit is further divided into four regions, consisting of 256 rows and columns for the top unit and 320 for the bottom, respectively. Each region also utilizes slightly different properties, for example, varied transistor values for the analog in-pixel front-end, which can lead to different threshold levels or noise contributions compared to other regions, useful for detector characterization and optimization purposes regarding later generations of sensors. Consequently, additional detectors were fabricated as leftover space was available on the wafers, which only consist of one of the repeating units and are, therefore, called BabyMOSS. The BabyMOSS consists of roughly 670000 pixels and is shown in detail in Figure 1.10. The in-pixel front end of the sensor is very similar to the DPTS but does not implement time-encoding for the hit position or energy information.

## 1 Introduction

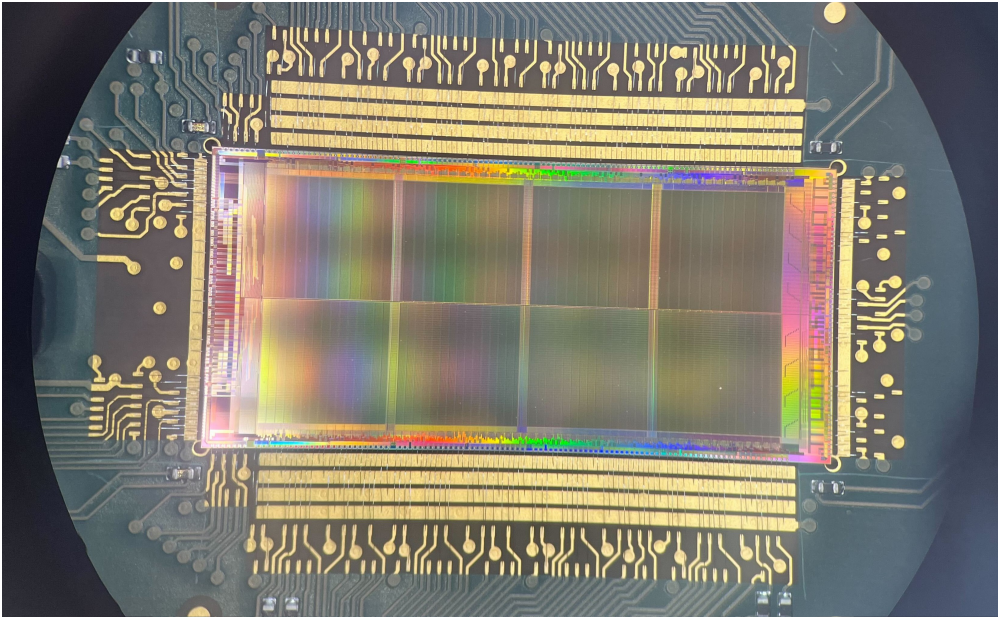


Figure 1.10: A close-up of the BabyMOSS sensor under the microscope, with all eight regions distinguishable.

## 2 Implementing an FPGA-Based Readout for Direct ToT-Measurement

### 2.1 DPTS Working Principle

#### 2.1.1 Decoding

As mentioned in chapter 1, the Digital Pixel Test Structure uses a time encoding approach to determine the pixel position within the matrix [30]. The exact procedure for this is depicted in Figure 2.1, showing the output of the DPTS through the CML (Current-Mode Logic) output in combination with the discriminator state.



Figure 2.1: A depiction of the pixel position- and the Time-over-Threshold encoding, involving two pulse trains and four pulses in total [26].

When an incident ionizing particle passes through the detector, a voltage signal is induced in the collection diode, which is amplified by an analog front-end stage. In the case that this signal is higher than the set threshold of the detector, the discriminator will be set to one, and the pixel will send out a first train consisting of two pulses. The first of these pulses has a fixed length of  $\approx 1$  ns. However, the difference between the rising edge of the first and the rising edge of the second pulse varies from pixel to pixel. This time is referred to as the PID (Pixel-ID) and defines the row position of the pixel. The information on the column position of the pixel is encoded in the duration of the second pulse of the train and is referred to as GID (Group-ID). The minimum difference between the PID time and the GID time is approximately 150 ps. Lastly, the information on the deposited or injected charge in the pixel is encoded by means of a second train of pulses sent out. This second train is of the same form as the first one and is sent when the analog signal falls below the threshold and

## 2 Implementing an FPGA-Based Readout for Direct ToT-Measurement

the discriminator is set to zero again. By taking the time difference between the first rising edge of each train, the Time-over-Threshold (ToT) is measured. Time-over-Threshold is a technique generally used in detector physics to measure the duration of a signal above a certain threshold, as illustrated in Figure 2.2. It can be used to determine the energy deposition within a detector, provided that the length of the signal is, to some extent, proportional or dependent on the amount of charge generated, as is the case for the DPTS.

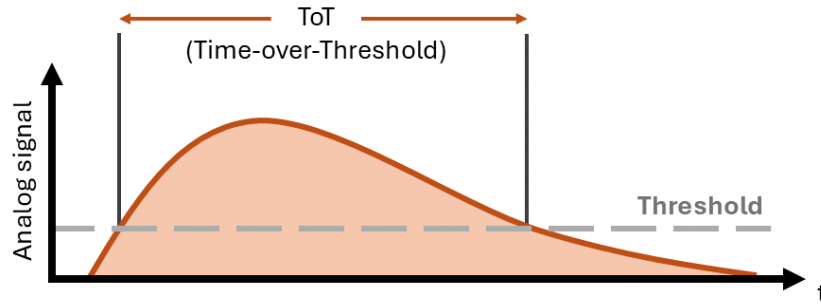


Figure 2.2: A sketch demonstrating how the ToT (Time-over-Threshold) of an analog signal is measured.

An example of some recorded DPTS signals (positive CML output) is shown in Figure 2.3. Depicted are the comparisons of the PID and GID waveforms between nearby pixels measured via the picoscope and the threshold set to 50 mV.

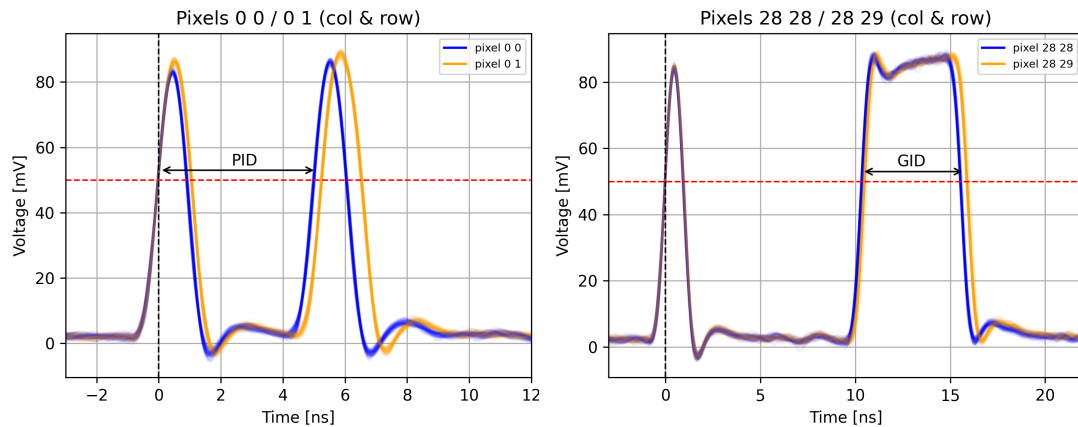


Figure 2.3: Different waveforms measured with the picoscope, demonstrating the difference of PID and GID for various pixels.

Since all pixels are connected to one single output line, there is the possibility of signal collisions when multiple pixels are firing. This, for example, happens when there is charge sharing among neighboring pixels. In order to minimize

## 2 Implementing an FPGA-Based Readout for Direct ToT-Measurement

the probability of collisions, the PID (ranging from 0 to 31) was inverted in every two columns. To mitigate the charge-sharing in the vertical direction, the PID was also ordered in a checkerboard pattern, as demonstrated in Figure 2.4. Moreover, adjacent columns inject the signals on opposite sides of a delay, which reduces the collisions in case of charge-sharing in the horizontal direction. Regardless of these strategies, hit transmission collisions, although rare, can still occur, in which case the data cannot be decoded.

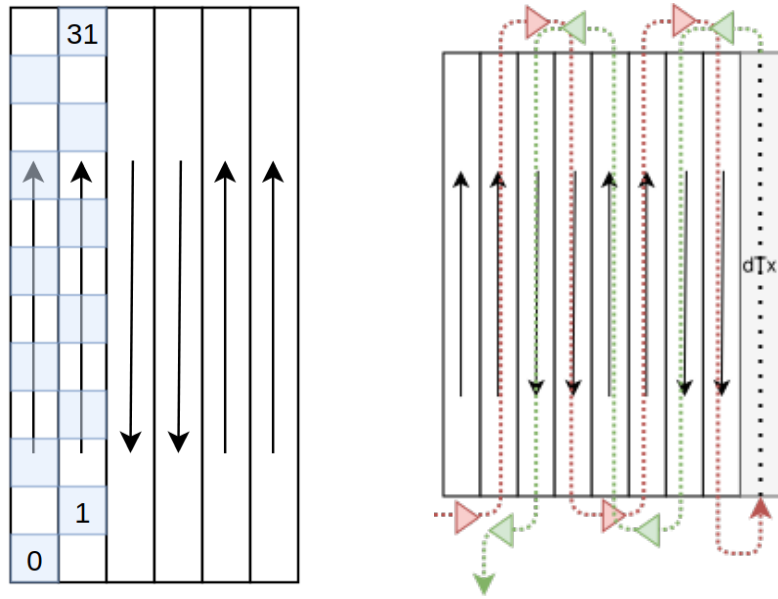


Figure 2.4: The pattern of the PID layout and the implementation of the column injection to the single digital output line.

The general setups used for the measurements with the DPTS are shown in Figure 2.5. On the left is pictured the setup employing the conventional readout method utilizing the PicoScope 6424E, which is a high-performance 4-channel PC oscilloscope with a bandwidth of 500 MHz and a sampling rate of up to 5 GS/s [31]. Since the DPTS has a differential output, it incorporates two lines (one positive and one negative), which have to be connected to the picoscope. Similarly to the BabyMOSS, the DPTS makes use of a DAQ board for data acquisition and communication with the chip. However, the jumper configuration is slightly different than that of the BabyMOSS, and the DAQ board has to be connected to the picoscope in order to trigger it. Between the sensor and the DAQ board is a proximity board, which converts the voltages and currents from the DAQ board to the desired values needed for operation. Pictured on the right is a part of the setup using the FPGA-based readout. The TRB3Sc board is powered via a power supply and connects to the output of the DPTS through two pins. The data transmission is implemented with a glass fiber cable, which is fed into a media converter (not shown in the picture) and

## 2 Implementing an FPGA-Based Readout for Direct ToT-Measurement

subsequently to the PC.

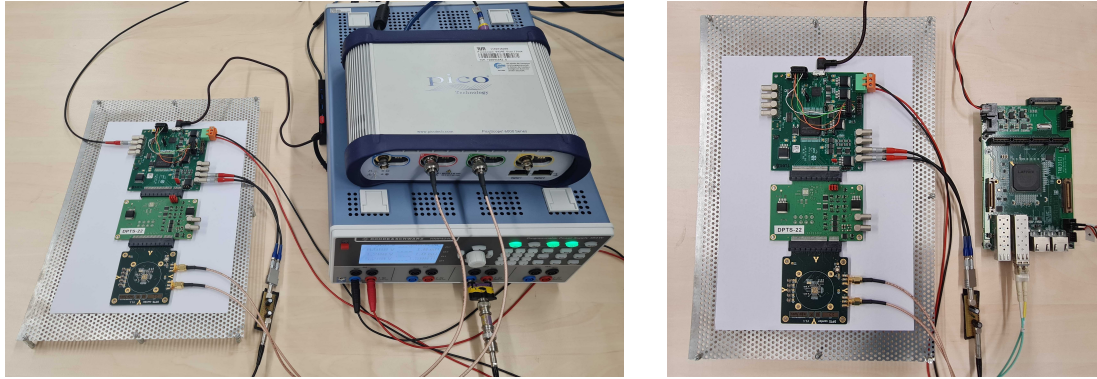


Figure 2.5: Left: The setup for the DPTS measurements using the picoscope as a readout. Right: A picture of the FPGA-based readout using the TRB3Sc board.

In order to assign the corresponding PID and GID to each pixel, a calibration is needed. This is achieved by pulsing each pixel 100 times and measuring the pulses using the picoscope for the readout. This results in a plot as shown in Figure 2.6.

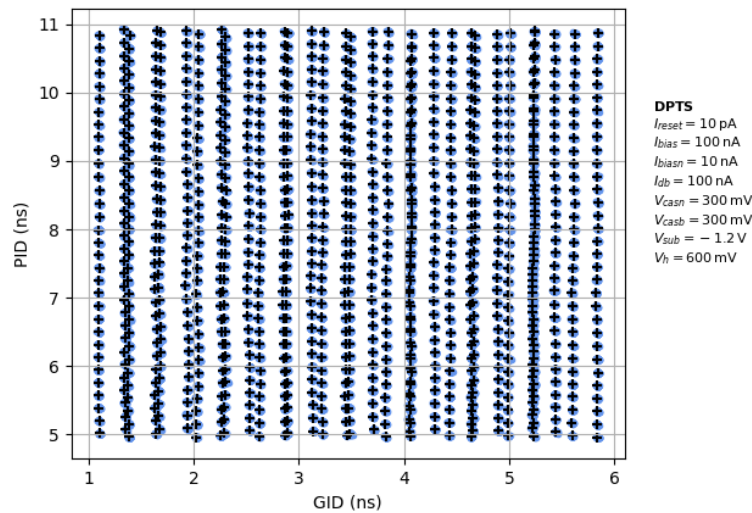


Figure 2.6: The PID and GID are plotted after pulsing each pixel 100 times and assigning a center of gravity.

For calibration, each pixel is assigned a Center of Gravity (CoG) of the 100 pulses, which can then later be used to determine to which pixel a signal belongs. Visible in the decoding calibration is that the PID and GID are not

precisely the same for train 1 and train 2 for numerous pixels, which is likely due to tiny differences in the delay chains that encode the PID and GID signals, dependent on whether the signal is generated at the rising or the falling edge of the analog signal. Therefore, the decoding for the first and second train are handled separately in the analysis. Additionally, the PID and GID can vary with changing settings, namely the applied back-bias voltage to the chip, as well as the temperature. Consequently, a decoding calibration should be performed for each measurement when one of these parameters changes.

### 2.1.2 ToT and Fake-Hit Rate

An essential aspect of the detector is the set threshold uniformity for the pixel matrix and the contribution of pixel noise. A dedicated measurement can be performed to quantify these points. A specific charge  $V_H$  is injected into each pixel 25 times using the injection capacitor, and it is then measured how often the pixel fired. Starting with a low injected charge, ideally below the threshold, the pixel will register zero hits. By gradually increasing the injection voltage, the pixel will start measuring hits until it sees 25 for values above the threshold, resulting in an 'S-curve' plotted in Figure 2.7.

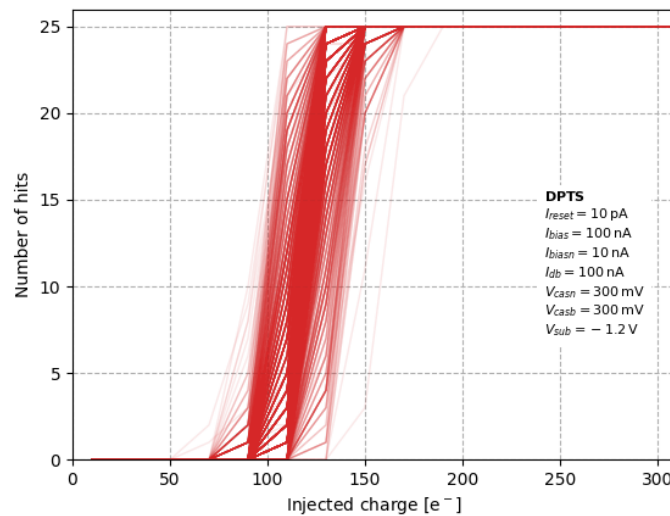


Figure 2.7: An S-curve outlining the threshold and noise of the pixel matrix.

To determine the threshold of each pixel, the derivative of the S-curve is taken, resulting in a distribution similar to a Gaussian. The mean of this Gaussian corresponds to the threshold value, while the width represents the noise contribution. Furthermore, this scan can be used to measure the Time-over-Threshold, which corresponds to a specific injection voltage. An example of this is shown in Figure 2.8.

## 2 Implementing an FPGA-Based Readout for Direct ToT-Measurement

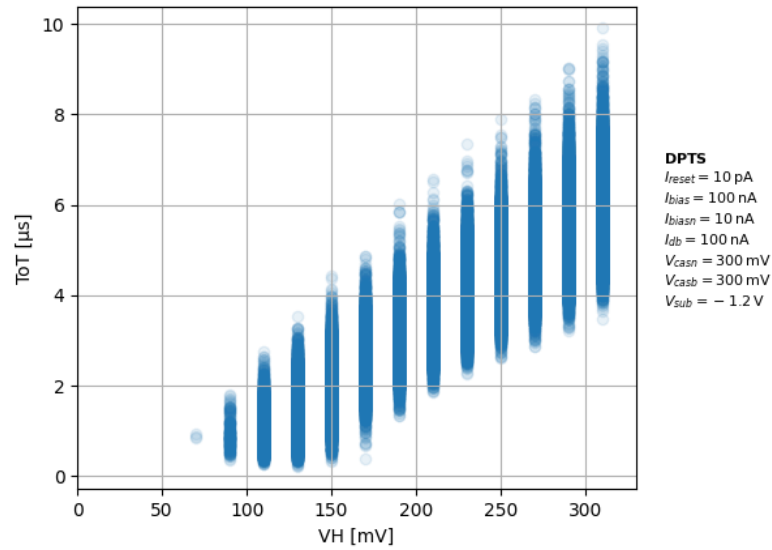


Figure 2.8: The Time-over-Threshold (ToT) as a function of the injected voltage  $V_H$ , including an example calibration curve for two pixels.

In the resulting curves, it is clear that there is a large spread of the ToT values for the same injection voltage. Due to this pixel-to-pixel variation, calibration is needed for converting measured ToT to collected charge, which is especially important for achieving a high energy resolution in, for example, source measurements. This is done by fitting a linear function (plus a deviation term for the low voltage region) to each pixel and saving the fit parameters for usage as a conversion for later analysis.

### 2.1.3 Energy Spectrum

As the DPTS was manufactured to specifically measure the energy deposition of particles passing through the detector, it is of great interest to demonstrate this feature and, therefore, to measure signals from a radioactive source to test the performance of the sensor. For this purpose, an  $^{55}\text{Fe}$  source was used as a particle emitter.  $^{55}\text{Fe}$  decays to  $^{55}\text{Mn}$  via electron capture of an electron in the inner shell and emits mainly X-rays of two energies. The  $K_\alpha$  X-rays with an energy of 5.89–5.9 keV stem from the electrons in the M-shell, which after the decay deexcite to the now empty place in the K-shell, generating a photon with the energy equal to the difference between the energy levels of the shells and a probability of 76.2%. Similarly, the  $K_\beta$  X-rays originate from electrons transitioning from the M-shell to the K-shell and releasing a photon in the process with an energy of 6.49 keV and a probability of 8.2%.

## 2 Implementing an FPGA-Based Readout for Direct ToT-Measurement

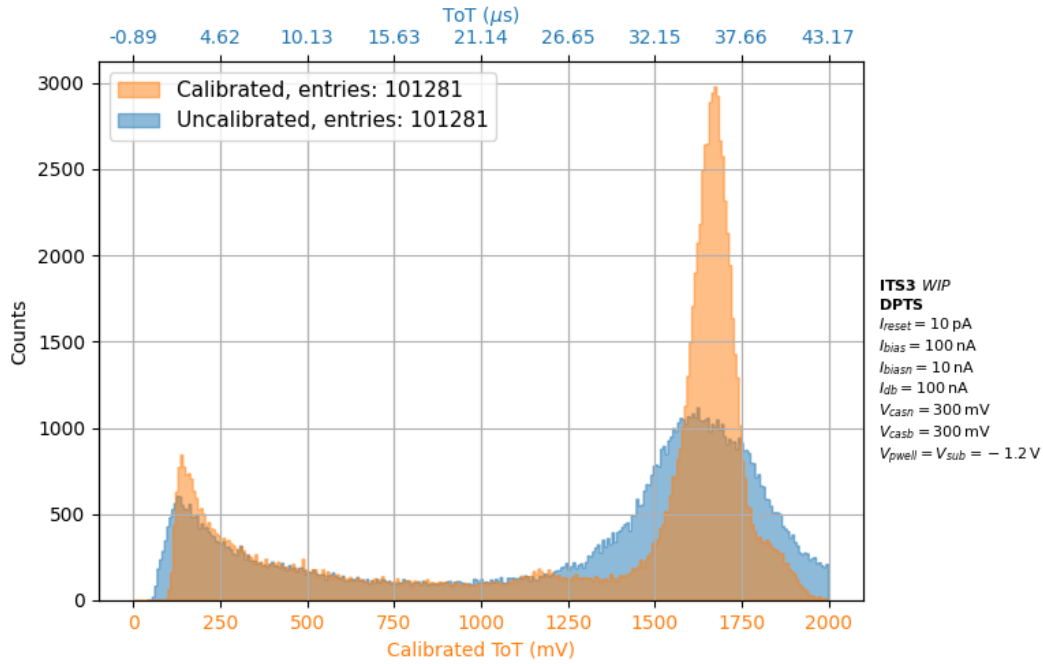


Figure 2.9: The measured  $^{55}\text{Fe}$  energy spectrum, both before and after applying the ToT calibration.

For the measurement, the iron source was placed at a distance of approximately 5 mm above the chip operated at default settings, and 1 million events were recorded. The decoding calibration is used to associate the signals to the correct pixel position within the matrix. Subsequently, the Time-over-Threshold values measured by the pixels can be plotted, as shown in Figure 2.9 in blue. Since the pixel-to-pixel variation of the ToT response is quite large, the energy resolution is not sufficient to resolve both the  $K_\alpha$  and  $K_\beta$  peak. Therefore, the ToT calibration can be taken into account. Using the acquired fit parameters from the calibration and converting the measured ToT in voltage for the specific pixels, one obtains a spectrum as shown in the orange histogram. After applying the calibration, the main  $K_\alpha$ , as well as the smaller  $K_\beta$  peak, can be clearly distinguished. Additionally, there are two smaller peaks visible at around 500 and 1200 mV, which can be identified as the silicon fluorescence and silicon escape peaks, respectively. These peaks arise due to the interaction processes of the X-rays with the silicon of the detector. The primary interaction that takes place is the ionization of silicon atoms, the majority of times an electron in the K-shell, through the photoelectric effect. This will lead to the emission of characteristic  $K_\alpha$  X-rays that are responsible for the silicon fluorescence peak, as an electron in the upper shells will fill the empty vacancy. However, it can happen that this characteristic X-ray leaves the detector without further interaction, which results in a peak with an energy equal to the difference of the energies of the Mn- $K_\alpha$  to Si- $K_\alpha$  X-rays.

## 2.2 FPGA-Readout TDC Implementation for Decoding

The DPTS has shown that the method of using a time-encoded hit position performs well for a detector of small dimensions with 1024 pixels. In particular, it demonstrates that the encoded Time-over-Threshold approach is possible and delivers excellent energy resolution when considering that the main function of the detector is for tracking purposes. Nonetheless, the current readout method utilizes a picoscope for decoding the signals. Taking into account the small size and pixel number of the sensor compared to full-scale experiment trackers, using a setup of multiple picoscopes as a readout is not feasible as this would require immense space, electronics, and resources. In this thesis, therefore, an FPGA-based readout is investigated, which would make it possible to employ detectors with a working principle similar to the DPTS in large-scale experiments.

An FPGA (Field-Programmable Gate Array) [32] is a type of integrated circuit that uses programmable logic blocks and can be repeatedly configured to a desired setup, which is typically done using a hardware description language, such as Verilog or VHDL. This makes FPGAs a versatile tool, as they are not permanently configured like conventional ASICs. The challenge that arises for utilizing this technology for the DPTS is, however, that the timing needs to be very precise in order to resolve the PID and GID values of the pixels. Since the difference between neighboring pixels is on the order of 150 ps or lower, the readout has to be able to measure on a precision of ideally tens of picoseconds or less. For that reason, the FPGA readout needs to have a high-precision TDC in order to measure accurate time differences. A TDC (Time-to-Digital-Converter) is a device or component used in electronics to measure times and convert them into a digital signal for further use.

The TRB3Sc (Trigger Readout Board) was selected as the readout electronics for the DPTS due to its suitability for the system's requirements. Developed as a complementary component to the TRB3, the TRB3Sc is a streamlined, single-FPGA variant of the TRB3. The original TRB3 was created at GSI in Darmstadt as a sophisticated data acquisition and control system featuring FPGA-based technology, and it is employed in experiments such as HADES. The TRB3Sc offers a compact solution for smaller, organized setups and can be modified so that it can be used on its own without the need for the TRB3 board. A picture of the TRB3Sc can be seen in Figure 2.10.

## 2 Implementing an FPGA-Based Readout for Direct ToT-Measurement

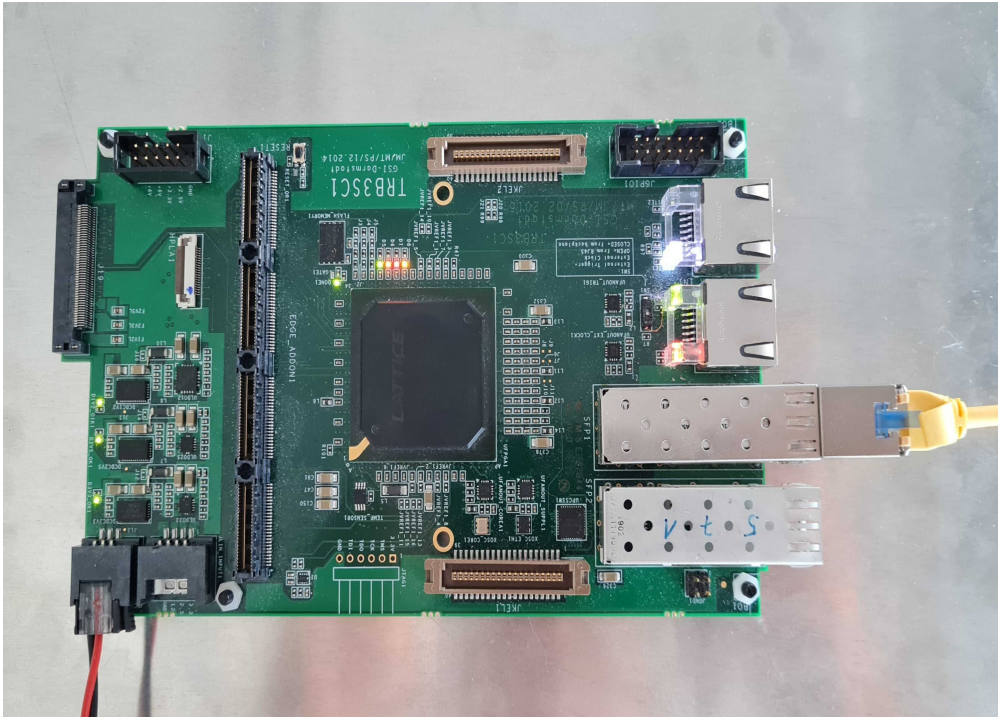


Figure 2.10: A picture of the TRB3Sc with implemented TDC-in-FPGA technology.

There are various different methods of implementing TDCs, which can be as simple as just counting clock cycles. This approach, however, limits the timing precision to the clock frequency so that a more sophisticated technique is needed to resolve and distinguish the signals produced by the DPTS. The architecture of the TDC used in the scope of this project comprises several building blocks. It makes use of a coarse counter, a fine time, an encoder, and a FIFO (First-In-First-Out) [33]. The coarse counter has a granularity of several nanoseconds and associates a general timestamp with each hit measured by the TDC. The measurement of a more precise time in the picosecond range is handled by the fine time measurement block, whose outcome is converted into a binary number through the encoder. Finally, the result is saved in a FIFO, which acts as a data storage. The fine time measurement is implemented using a Tapped Delay Line (TDL). A Tapped Delay Line incorporates a sequence of delay elements along its path, ideally all with a similar propagation delay. The basic measuring principle of a signal is now to sample the state as it propagates through the line. By checking how far the signal traveled, the time can be determined with very high precision, limited by the length of the propagation delays [34].

## 2 Implementing an FPGA-Based Readout for Direct ToT-Measurement

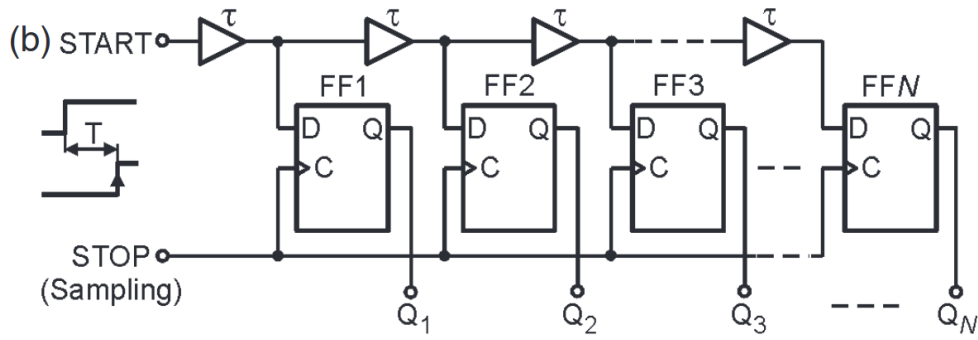


Figure 2.11: An example of a Tapped Delay Line. [34]

A total of three TDCs are implemented in the FPGA to decode the DPTS signals. A sketch of how the measurement of PID and GID are realized is shown in Figure 2.12, with a combination of TDCs, which are enabled and disabled by the logic of four flip-flops. This produces three measured times per event (per train), decoded by subtracting the TDC times from one another, resulting in the desired PID and GID values. The PID is achieved by subtracting the measured time for each hit of TDC0 from TDC1 and GID by subtracting TDC1 from TDC2. It has to be noted that the GID time is not the same as the one measured by the picoscope, as the implemented logic introduces some delays. However, this does not affect the results as for the decoding; only the relative time between pixels is important, and not the absolute GID time, which is approximately 1 ns longer with the FPGA readout.

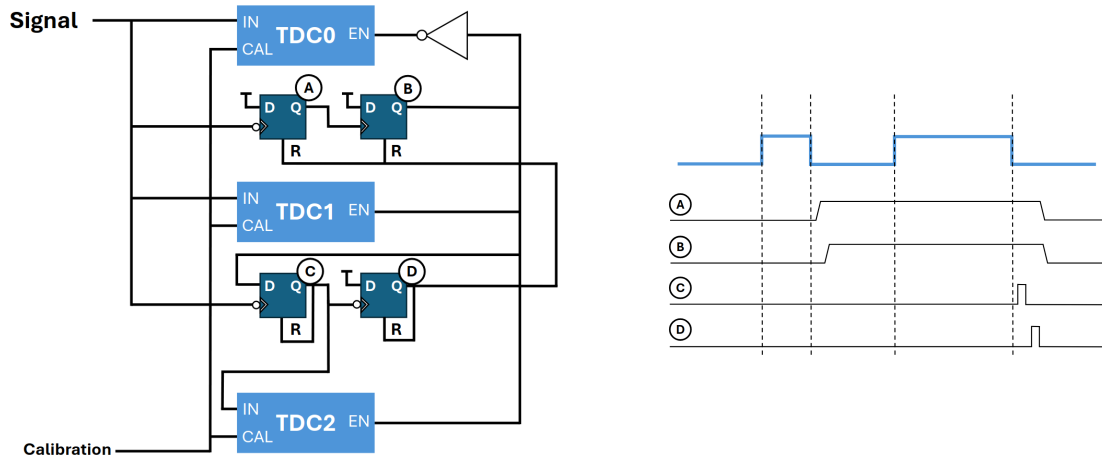


Figure 2.12: A sketch of the TDC implementation and the flip-flop logic used to decode the DPTS signals.

As mentioned, the TDC precision depends on the delay elements in the delay line. Since these are not always the same and can have non-linearities, the bin width of the TDC can also vary. In this case, the width of the bins is in the range

## 2 Implementing an FPGA-Based Readout for Direct ToT-Measurement

of 3 to 30 ps. This is well within the margin that is required for the accurate decoding of DPTS signals. TDC calibration is performed by analyzing a large number of hit signals assumed to be random and uniformly distributed across the clock period. This statistical approach allows the determination of the actual bin widths. These calibrated time values are then stored in a Look-Up Table (LUT), which is a data structure that provides quick access to pre-computed results. These values are then applied to the subsequent measurements, thereby improving the precision. An example of a calibrated curve for the three TDCs (0-2) is shown in Figure 2.13. An important property of the TDCs is that the temperature affects the calibration of the fine time and can, therefore, deteriorate the precision [35].

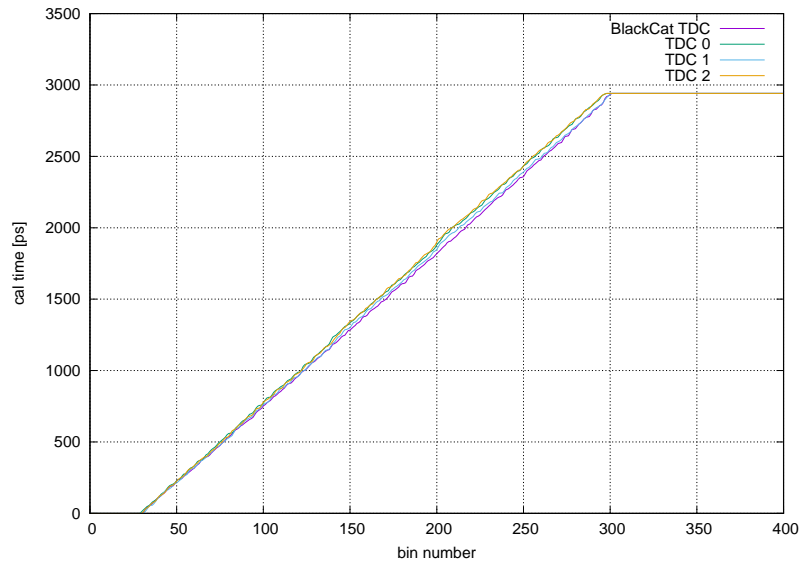


Figure 2.13: The measured calibration time as a function of the bin width for the three TDCs.

What has to be noted is that in the implementation used for these studies, the rate at which data can be taken is, to some extent, limited by the occurrence of signal collisions and synchronization errors among the TDCs. This is not inherent to the readout itself and can be modified by adding the following improvements: a gathering mechanism to combine data from TDC FIFOs into a single large FIFO, a round-robin method to ensure synchronization between TDCs, a network-forwarding configuration with an assigned IP, MAC, and port, and a connection to a data forwarder where the data is written to a file, and a decoder tool to convert raw data into times and apply calibration. This type of readout is already used by other applications and was only not implemented

for the DPTS due to limited time, but is, in principle, viable.

## 2.3 Performance

After confirming that the FPGA and TDCs are functioning correctly based on previous tests, the next step involves thoroughly assessing the performance of the readout. This includes comparing necessary performance measures such as signal decoding, ToT measurements, and energy resolution with the original readout setup that utilized the oscilloscope. By conducting these comparisons, we aim to determine if the FPGA readout meets or exceeds the previous system's performance standards and identify any potential improvements. Due to the slower data taking with the readout version used in these studies, the pulsing measurements were carried out with fewer pulses than the oscilloscope scans, which should nonetheless not affect the performance comparison as still enough statistics were gathered across all pixels.

The first and most crucial test that needed to be done was to verify that the readout could reliably measure the PID and GID of the pixels with sufficient precision to distinguish the signals of neighboring pixels. This was investigated by performing a decoding calibration similar to the one obtained via the oscilloscope. The decoding is shown in Figure 2.14 and was done by pulsing each pixel 25 times while measuring the PID and GID. The crosses mark the centers of gravity and can be clearly distinguished for the different pixels, demonstrating that the FPGA-based readout is capable of identifying single pixels consistently. The decoding calibration is equivalent to the oscilloscope measurement, with a difference seen towards the edges of the graph where a wave-like pattern is observed. However, this does not seem to deteriorate the performance in decoding different pixels and most likely stems from the readout electronics, such as the additional cables, connections, and the TDCs themselves, or from a slight miscalibration of the TDCs due to temperature variations during the measurements.

## 2 Implementing an FPGA-Based Readout for Direct ToT-Measurement

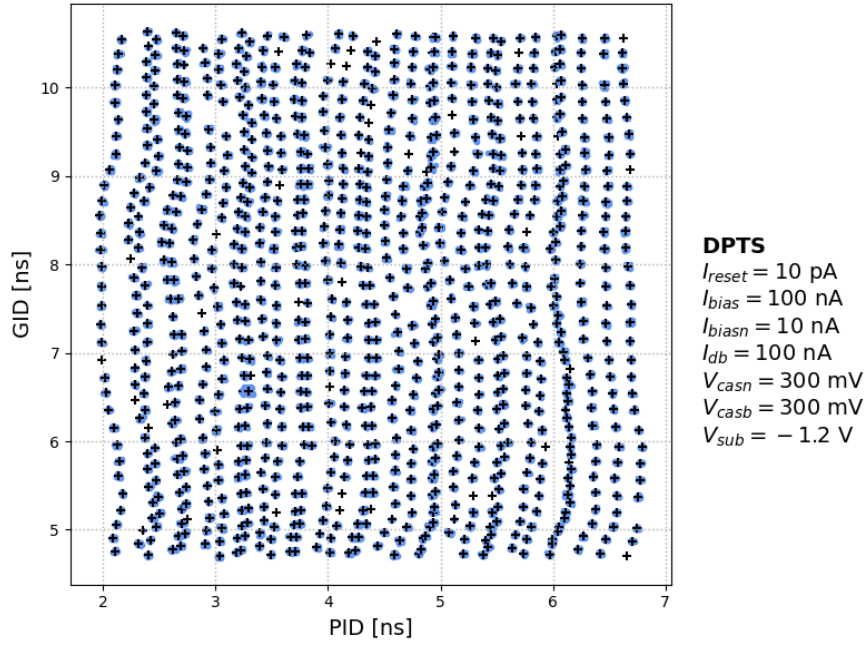


Figure 2.14: The decoding of the DPTS signals, obtained using the FPGA-based readout. It shows the measured PID and GID, as well as the center of gravity for each pixel.

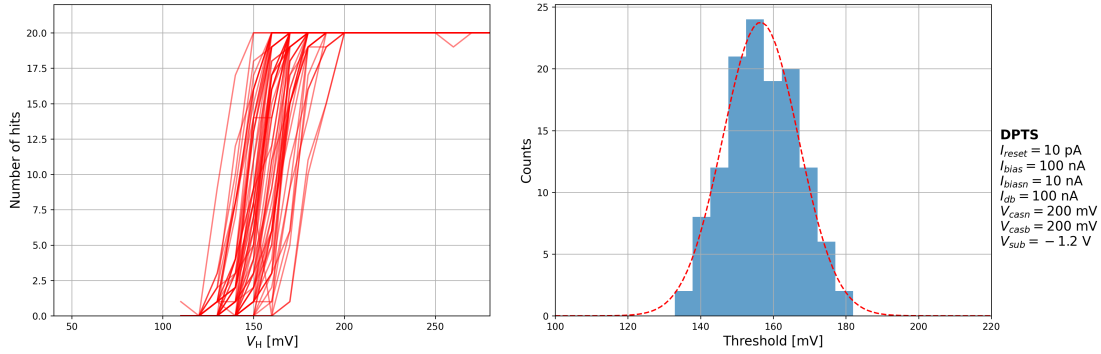


Figure 2.15: Left: The S-curve obtained by performing a threshold scan for four rows with the FPGA-based readout. Right: The threshold distribution of the pixels fitted with a Gaussian.

A threshold scan was performed to test the capability of the FPGA readout to measure the threshold. In total, four rows were scanned, totaling 128 pixels. Each pixel was pulsed twenty times for different injection voltages, ranging from 110 to 280 mV in steps of ten. For this specific measurement, a different variant of DPTS, the DPTS-O, was tested. It does not incorporate the cross-connect for the pixel position encoding as the DPTS-X variant, which was used for all other

## 2 Implementing an FPGA-Based Readout for Direct ToT-Measurement

measurements. The produced s-curves are shown on the left in Figure 2.15. The shape generally looks compatible and similar to the curves obtained via the oscilloscope. Some decoding errors were occasionally observed, visible as pixels with a significant dip in the number of hits recorded. Therefore, pixels with entries of less than 19 hits significantly above the approximate threshold were rejected for the threshold analysis and are not shown.

The threshold for each pixel is calculated by numerically estimating the derivative, similar to what is done for the oscilloscope data. The threshold distribution is shown on the right plot in Figure 2.15. By fitting a Gaussian, the mean threshold of the matrix is calculated and equals to around 156.6 mV. The average noise is given by the width of the Gaussian of 10.4 mV. The threshold of the sensor was manually increased by setting  $V_{CASN}$  and  $V_{CASB}$  to 240 mV to mitigate noisy pixels so that the measured threshold value meets the expectations.

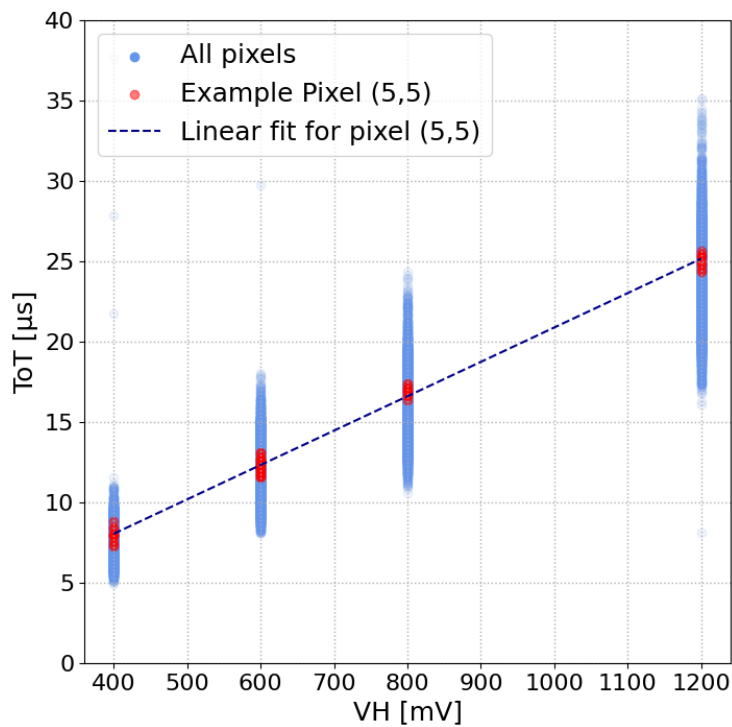


Figure 2.16: The ToT response as a function of the injection voltage  $V_H$  measured with the FPGA-based readout, including a linear fit for a pixel (5,5).

For the following measurements, only the default values of the DPTS were used. The Time-over-Threshold calibration that was conducted with the FPGA-based readout is shown in Figure 2.16. Each pixel is pulsed 20 times, and the

## *2 Implementing an FPGA-Based Readout for Direct ToT-Measurement*

ToT is measured. This is repeated for different injection voltages  $V_H$  ranging from 400 to 1200 mV. The calibration for the specific pixels is realized by fitting a linear function to the pixel data, which gives the relation of ToT to the collected charge. To decode the ToT from the measured data, the 'absolute' time that is stored with each hit is used. By grouping the hits in groups of two and subtracting the times, the ToT is obtained. The performance of the calibration with the FPGA readout is equivalent to the oscilloscope readout and was tested with a source measurement.

Again, the source measurement was done utilizing the  $^{55}\text{Fe}$  source. The DPTS signals are recorded and decoded using the FPGA readout, giving the measured PID and GID to associate hits with pixels. Unlike pulsed measurements, where the signals are evenly spaced, in source measurements, a signal from pixels can occur in the time frame of ToT of another pixel. Since these hits are more likely to stem from charge-sharing and cluster size  $> 1$  events, they are rejected in the analysis. This is generally done because events with charge sharing deteriorate the energy resolution since the generated charge is collected by one pixel and split up between multiple. The resulting energy spectra are displayed in Figure 2.17. Apart from the FPGA readout results, the spectra obtained with the oscilloscope are also shown for comparison, both for the uncalibrated case and for the calibrated spectra, in which the ToT calibration for each pixel was applied.

## 2 Implementing an FPGA-Based Readout for Direct ToT-Measurement

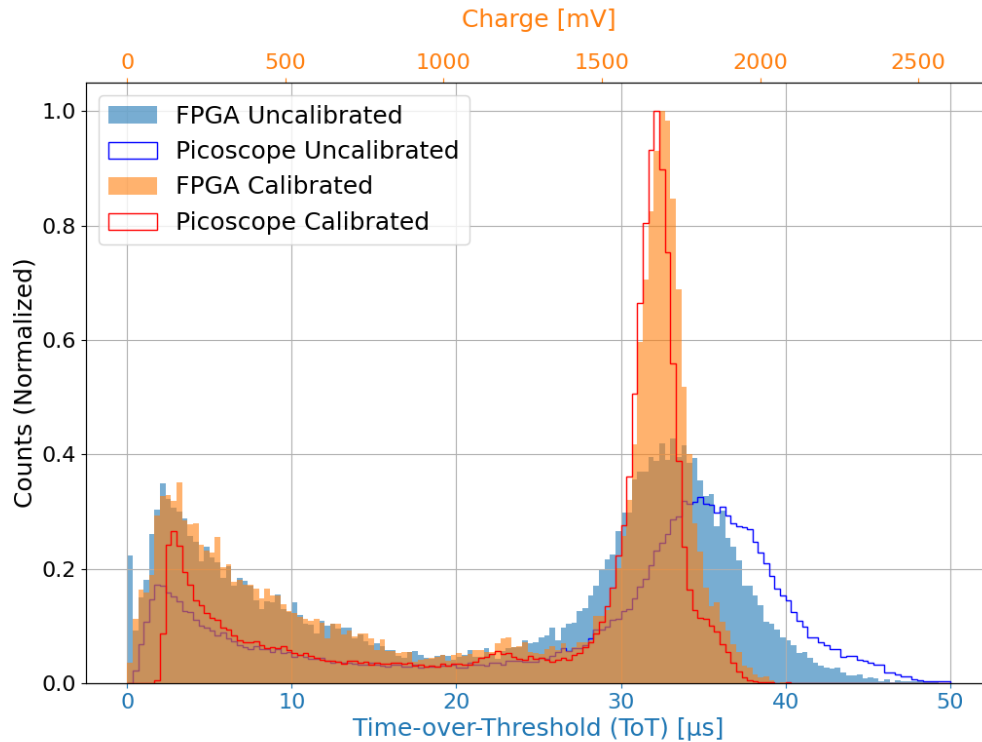


Figure 2.17: A comparison between the picoscope and the FPGA-based readout between the calibrated and uncalibrated  $^{55}\text{Fe}$ -spectra.

Considering only the FPGA readout spectra, it is clearly seen that the previous ToT calibration was successful and that after applying the calibration, the resolution of the main peak drastically increases and that, for example, the silicon escape peak can be noticed at around  $23\ \mu\text{s}$ . However, the  $K_{\beta}$ -peak next to the main  $K_{\alpha}$ -peak is hardly resolved in comparison to the picoscope measurement. It is also observed that there is a slight shift between the readout methods for the uncalibrated data, which is not fully understood. A possibility could be different outside parameters and changes, such as temperature or a variation of the chip and electronics itself since several months lay between the two measurements.

The most significant difference between the spectra is the increased height towards lower ToT for the FPGA-based readout. A reason for this could be that these signals stem from events with considerable charge-sharing, likely with a cluster size above one. This suggests that the method of filtering out these attempts did not fully work and has to be revised since this also affects the energy resolution.

## 2 Implementing an FPGA-Based Readout for Direct ToT-Measurement

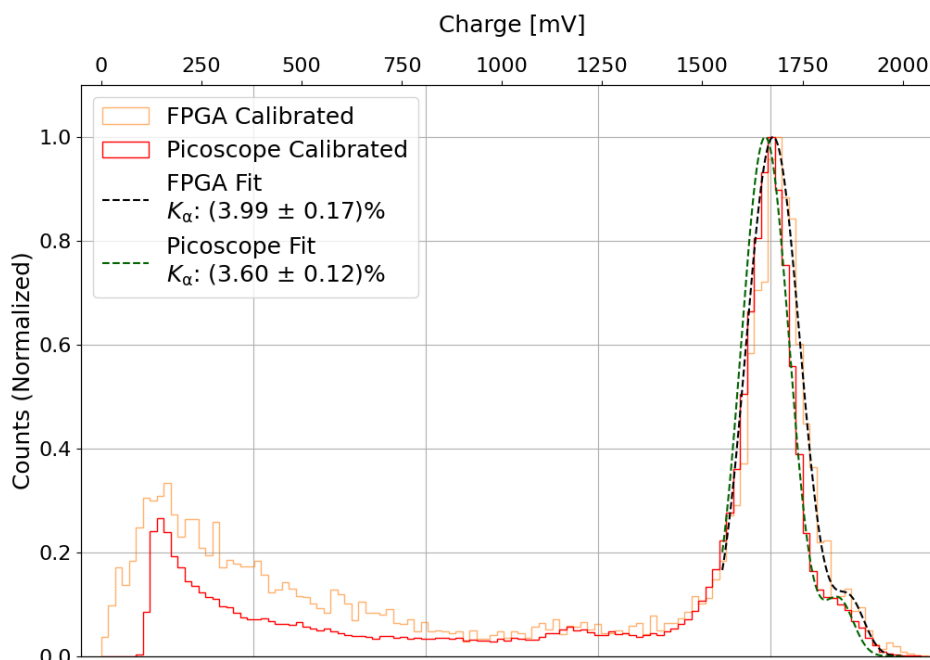


Figure 2.18: A comparison between the picoscope and the FPGA-based readout between the energy resolution of the calibrated  $^{55}\text{Fe}$ -spectra.

In order to compare the performance of the different readout methods regarding the energy resolution, the main peak/s of the iron spectra were fitted with Gaussians. The picoscope data clearly displays the second  $K_\beta$ -peak so that two Gaussians were used to fit the spectrum in a range of 1550-2000 mV. The FPGA readout data does not have a pronounced second peak but was nonetheless still fitted with two Gaussians to better compare the different readout methods. The values of the energy resolutions are given in Table 2.1.

	$K_\alpha$ -peak	$K_\beta$ -peak
Picoscope	$(3.60 \pm 0.12) \%$	$(1.96 \pm 0.87) \%$
FPGA	$(3.99 \pm 0.17) \%$	$(1.98 \pm 1.88) \%$

Table 2.1: The energy resolutions of the  $K_\alpha$  and  $K_\beta$ -peak for both readout methods.

As expected, the  $K_\beta$ -peaks have a significant uncertainty for both readouts, especially for the FPGA readout, as fitting a single Gaussian to the data is more favorable. As mentioned, this was done deliberately to better compare the  $K_\alpha$ -peaks, which have similar resolution, albeit worse with the FPGA readout. The

## *2 Implementing an FPGA-Based Readout for Direct ToT-Measurement*

difference is roughly 10%. This can be attributed to the possible charge sharing, the slightly lower statistics, and the fact that data-taking was performed over a longer time span with the FPGA-based readout, so environmental changes could have affected the performance.

Overall, the implemented FPGA-based readout shows comparable performance in almost all aspects and is capable of measuring with a timing resolution equivalent to the picoscope readout.

# 3 ToT-Measurement with Digital Oversampling

## 3.1 Oversampling Method

As described earlier in chapter 1 and 2, ToT measurement is normally not a built-in feature in full-scale MAPS detectors. Nonetheless, there are still ways to obtain information on energy deposition, such as digital oversampling of analog signals.

In the case of particle trackers, the term sampling typically refers to recording a hit signal generated by the particle within a specified time interval. This time interval is defined by the sampling period and strobe length, which are the duration during which the detector's electronics are actively monitoring for signals. The sampling period is commonly set to several microseconds to ensure that signals are sampled most of the time only once, therefore preventing excessive data output. Setting the strobe length and sampling period to a very short interval can increase the number of samples taken, potentially leading to multiple samples per hit. This is generally undesirable because it increases the data volume that must be processed and transmitted, which can slow down or overwhelm the readout electronics.

Moreover, in most particle tracking applications, the primary goal is to obtain binary hit information, which means indicating whether a particle passed through the detector. Since each particle passing through the detector should ideally generate one hit, sampling the signal once per hit is sufficient. An example of this is shown in Figure 3.1, whereby regardless of the signal height and shape, the hit is only sampled once.

### 3 ToT-Measurement with Digital Oversampling

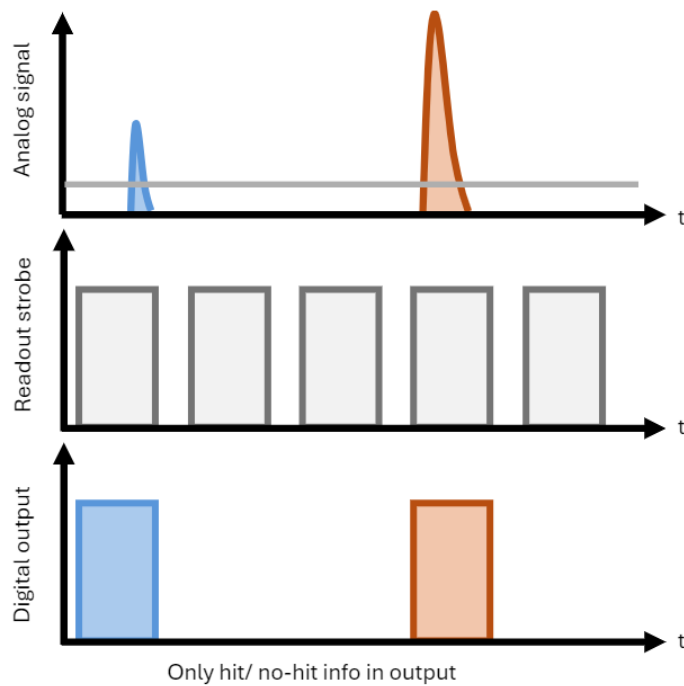


Figure 3.1: An example of how different signals are sampled exactly once, using an appropriate sampling period.

Nevertheless, there is still an application for so-called oversampling, in which the strobe length and sampling period are set to a concise length in order to record multiple hits per signal. The basic principle of oversampling is pictured in Figure 3.2. Depending on the length and height of the signal, the amount of sampled hits, and therefore the measured ToT, will be different.

### 3 ToT-Measurement with Digital Oversampling

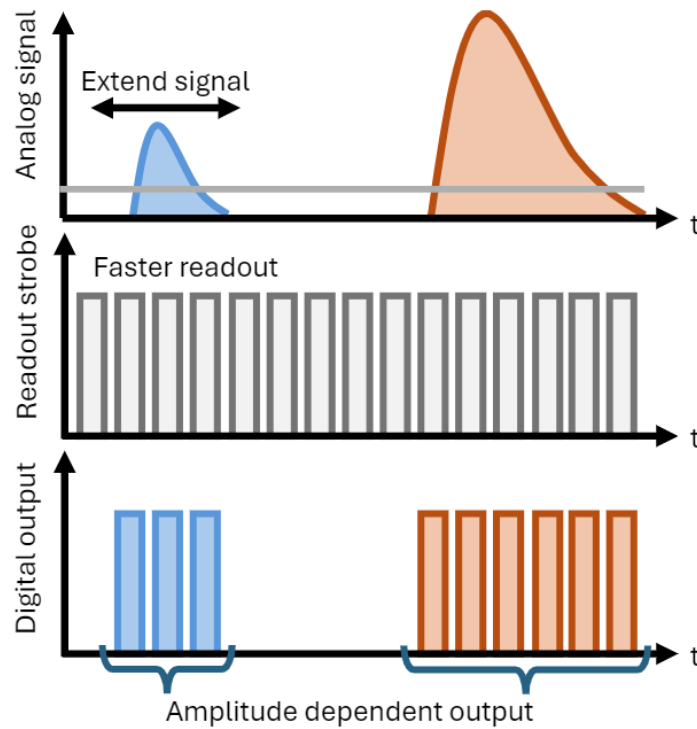


Figure 3.2: An illustration demonstrating how oversampling is used to measure ToT and distinguish signals of varying shapes. [36]

This method was already demonstrated with MAPS detectors, using the ITS2 of the ALICE experiment [36]. The ALPIDE sensors of the tracker incorporate a voltage parameter called  $V_{\text{Clip}}$ , which is used to truncate the signal, preventing it from being oversampled and ensuring that only the presence or absence of a hit is recorded. However, the  $V_{\text{Clip}}$  can also be set to a high value, in which case the charge dependency of the signal can be measured. This, paired with adjusting the sampling period to a comparably short duration, allows the ToT and energy deposition to be determined [37]. An example of one of these color runs is displayed in Figure 3.3. It shows the measured energy loss  $dE/dx$  in the inner barrel of the tracker as a function of the track rigidity, meaning momentum divided by charge. Considering particle identification (PID), the oversampling method demonstrates that different particles, such as kaons, pions, and protons, can be distinguished using a binary readout MAPS.

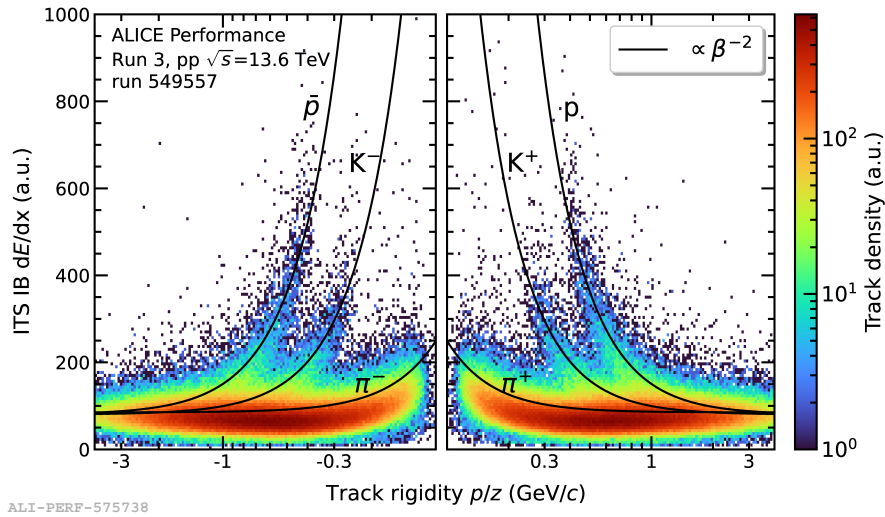


Figure 3.3: An energy loss measurement performed with ALICE using the oversampling method with ALPIDE chips. [36]

## 3.2 Tests with BabyMOSS

### 3.2.1 Source Measurements

The BabyMOSS laboratory measurements were performed using the setup as shown in Figure 3.4. The DAQ (Data Acquisition) board is visible on the right side, is connected to the PC by USB, and handles the communication with the chip while supplying the necessary power. A HAMEG power supply powers the DAQ board itself. However, placing an additional jumper is also possible to power the board solely via USB. An extra cable can be connected from the board to the power supply to operate the detector with back-bias voltage, including a filter board that reduces the noise and ensures a stable voltage supply. A zero-ohm shunt should be used when operating without back bias to avoid a floating connection.

A so-called Raiser card is placed between the DAQ board and the sensor. It converts the voltages and currents supplied by the DAQ board to the necessary values for operating the detector. Connected to the Raiser card is finally the carrier card on which the BabyMOSS is mounted. It is screwed into a metal case with a lid to shield the sensor from light. For source measurements, the radioactive sources can be placed into the lid, pointing toward the sensor and irradiating it at a distance of roughly 5 mm.

### 3 ToT-Measurement with Digital Oversampling



Figure 3.4: A picture of the BabyMOSS setup used for testing the sensor and performing source measurements.

For all the scans, only one region of the chip is enabled. Otherwise, valuable readout time is lost, which extensively increases the measurement duration as it leads to incomplete events in case a new trigger arrives while the sensor is being read out. As for the settings, the strobe length is set to 5 clock cycles, which corresponds to 150 ns with a sampling period of roughly 4  $\mu$ s.

The oversampling source measurements are also performed with an  $^{55}\text{Fe}$  source. Since the resolution limit with oversampling is determined by the sampling period, only the main peak of the spectrum can be resolved. An example of measured ToT-spectra for two different parameter settings is shown in Figure 3.5. The plots display the number of events with a certain number of consecutive sampled hits and summed up every 4  $\mu$ s, and therefore the Time-over-Threshold.

### 3 ToT-Measurement with Digital Oversampling

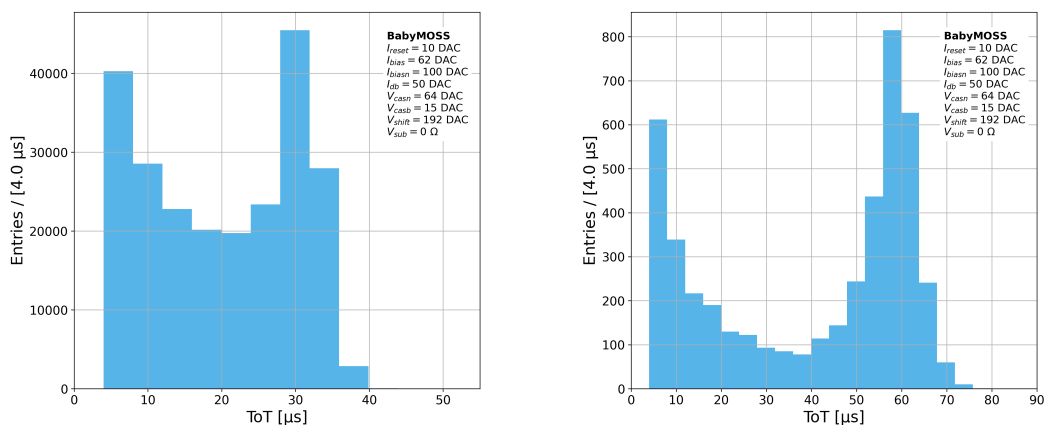


Figure 3.5: Energy spectra obtained with an iron source using different settings, thereby changing the signal length and threshold.

The main parameters that were investigated are  $I_{\text{RESET}}$  and  $V_{\text{CASB}}$ , which influence the analog signal length and the pixel threshold, respectively. The left plot in Figure 3.5 uses the default values  $I_{\text{RESET}} = 10 \text{ DAC}$  and  $V_{\text{CASB}} = 15 \text{ DAC}$  for the operation without back-bias voltage ( $0 \Omega$  resistor). In the right plot, the  $I_{\text{RESET}}$  value was changed to 4 DAC. As expected, decreasing  $I_{\text{RESET}}$  extends the signal and increases the overall ToT from  $30 \mu\text{s}$  to roughly  $60 \mu\text{s}$ .

A Gaussian plus linear background is fitted to the ToT distributions to estimate the position of the main peak, as illustrated in Figure 3.6. Since the binning is relatively coarse and the fit is only calculated for five bins, the fit uncertainty can, in some cases, not be estimated. As a cross-check, the main peak position was also calculated by taking the mean of the bin with the highest count and the neighboring bins. Additionally, the same was done where the next-to-neighboring bins were included. All three methods lead to similar results for the peak positions. Therefore, the Gaussian fit method is used to compare how different parameters influence the ToT behavior of the BabyMOSS. Taking the standard deviation  $\sigma$  and the mean peak position  $\mu$ , the energy resolution is calculated for each peak using the relation:

$$E_{\text{Res}} = \frac{\sigma}{\mu}. \quad (3.1)$$

### 3 ToT-Measurement with Digital Oversampling

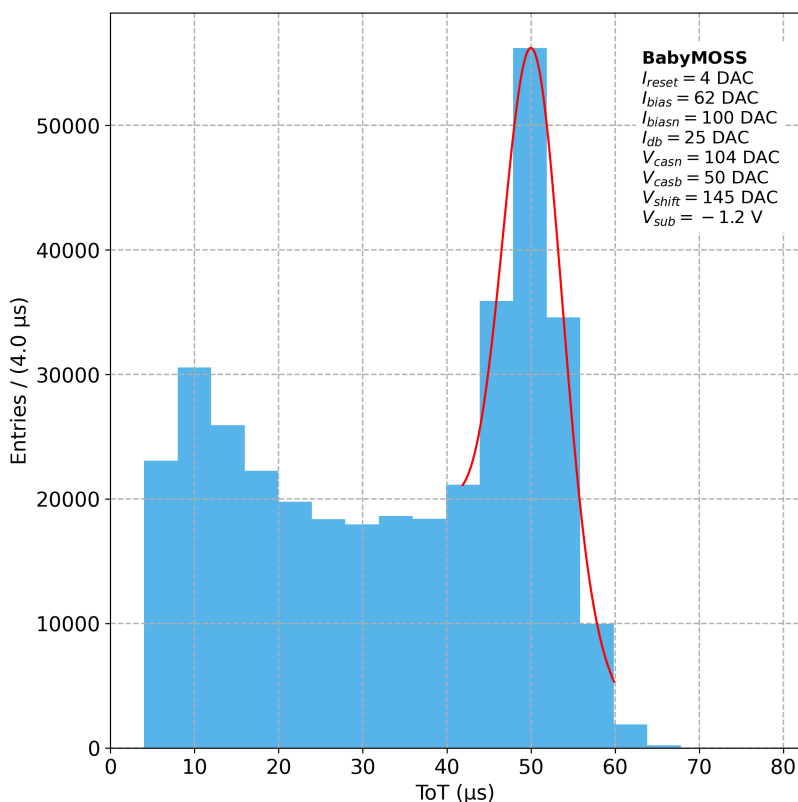


Figure 3.6: The ToT distribution with a Gaussian fitted to the main peak of the spectrum.

Using the fits, the analog signal shape from the pixels can be probed and estimated. This is realized by performing multiple ToT scans at different  $V_{CASB}$  values and, therefore, different thresholds. In order to convert the  $V_{CASB}$  into a threshold, a threshold scan is carried out at the same settings as the associated ToT measurement. The threshold values are given in DAC units as a conversion to mV or  $e^-$  requires additional calibration and measurements. Due to limited time, this was not performed and was also not necessary as the goal was to only qualitatively probe the signal. The result is plotted in Figure 3.7. The threshold is shown as a function of the main peak position and for three different values of  $I_{RESET}$ . The first observation is that, again,  $I_{RESET}$  influences the general positioning of the main peak. It can also be seen that the ToT response is linear for the full range of threshold values. However, the absolute slope of this linear behavior varies for different  $I_{RESET}$  and tends to lessen with decreasing  $I_{RESET}$ . This suggests that, as expected, the signal shape has a linear behavior within the probed threshold range and that the corresponding slope is dependent on  $I_{RESET}$ , which therefore does not only alter the signal length but also slightly the signal shape.

### 3 ToT-Measurement with Digital Oversampling

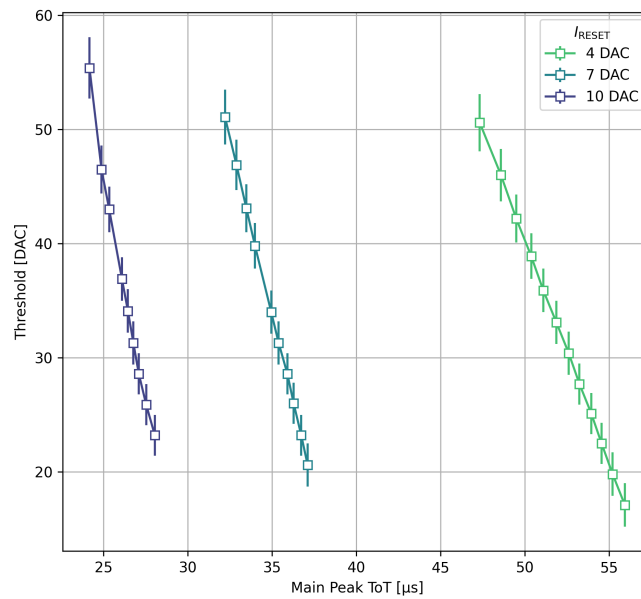


Figure 3.7: The measured threshold as a function of the main peak position, plotted for different values of  $I_{\text{RESET}}$ .

Since the source measurement can not be carried out with a shorter strobe length and sampling period, the resolution and binning are restricted to the  $4 \mu\text{s}$  sampling period. Another factor limiting the resolution is the pixel-to-pixel variations of the ToT response, which is illustrated in Figure 3.8. It shows the mean ToT values for pixels with at least 200 hits from the iron source. This pixel dependency can be taken into account by performing a pixel-specific ToT calibration.

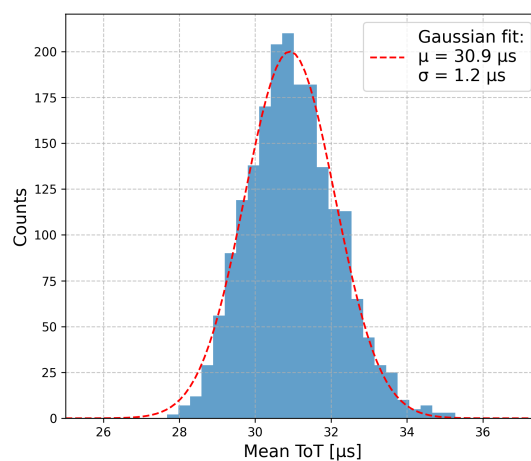


Figure 3.8: The mean ToT distribution for various pixels to demonstrate the pixel-to-pixel variation, fitted with a Gaussian.

### 3 ToT-Measurement with Digital Oversampling

To achieve calibration, we conducted an extended measurement using an X-ray source over the weekend to gather sufficient statistics for each individual pixel. The calibration aims to determine the position of the primary peak produced by the iron source for each pixel. Since the energy corresponding to the main peak of  $^{55}\text{Fe}$  is well known—around  $1640\text{ e}^-$ , this value can be used to convert the measured Time-over-Threshold at the peak to the corresponding charge in electrons. By fitting a linear function between the origin (0,0) and the estimated peak ToT value at  $(E_{\text{Fe}}, \text{ToT})$ , a ToT-to-electron conversion function is established for each pixel. This is possible under the assumption that the ToT response behaves approximately linearly with the deposited charge.

In order to avoid biasing the data through pixels that lack statistics, a cut was made to include only pixels with a hit count of more than 30. Additionally, to exclude noisy pixels from the analysis, the mean peak position was calculated by taking the mean of the ToT distribution only for values above  $30\text{ }\mu\text{s}$ , as the position of the peak is known to be in the range of  $40\text{-}50\text{ }\mu\text{s}$  for the settings used.

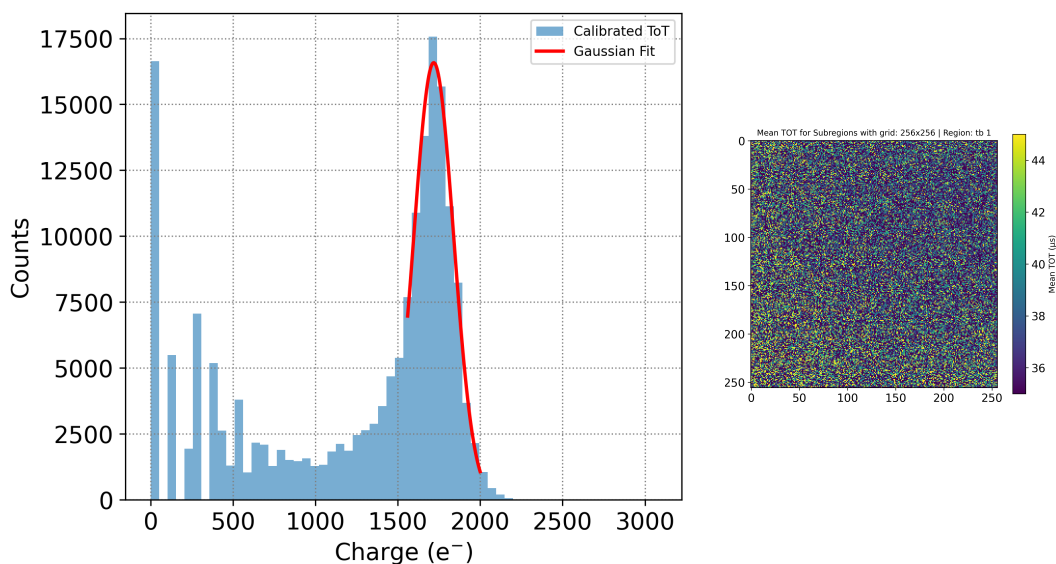


Figure 3.9: Left: The pixel-by-pixel calibrated  $^{55}\text{Fe}$ -spectrum in terms of deposited charge with a Gaussian fitted to the main peak. Right: The ToT distribution of all pixels for the performed source scan used for calibration.

The recorded mean ToT data for each pixel is shown in the 2D histogram in Figure 3.9. The pixel-to-pixel variation can be clearly seen, with a varying mean ToT value of roughly  $36\text{-}44\text{ }\mu\text{s}$ , and is again seen to be independent of the position in the pixel matrix as a uniform and 'random' distribution is observed. The final calibrated spectrum using the same data as the calibration

itself is shown in the other plot. As a final filtering step, only pixels whose slope of the fit function lies within three sigma of the average slope of the calibrated pixels are shown. It is observed that calibration worked partially, as the main peak is clearly visible and in the expected range for the X-ray source. To check if the calibration actually improved the energy resolution in comparison to the uncalibrated case, a Gaussian is fitted to the main peak. This results in a value of  $\approx 7\%$  for the standard deviation divided by the mean, which is comparable with the resolution that is obtained without calibration (7-8%). Therefore, the calibration process has to be reevaluated, as no significant improvement is observed. Nonetheless, this method could still be improved with, for example, higher statistics and additional points of known energy for pixel-by-pixel calibration.

#### 3.2.2 Test Beam Measurements

One of the most important tests that need to be performed with newly developed detectors and prototypes is beam tests. In a beam test, the detector that needs to be studied is placed in line or near a particle beam to study the general performance of the detector and imitate conditions similar to 'real' experiments. A configuration that is often used to conduct a test beam is a beam telescope. In such a setup, the studied detector, also called DUT (Device Under Test), is placed in the beamline and typically incorporates reference detectors in front and behind the DUT, whose performance is well-known.

The BabyMOSS is a relatively new prototype that has yet to be extensively studied. As such, further test beams are necessary to thoroughly characterize its performance and optimal operating points. Initial test beams have been conducted using a single BabyMOSS detector as the DUT, with ALPIDE sensors serving as reference planes. We, therefore, participated in a test beam campaign in July 2024, in which BabyMOSS sensors were used not only as the DUT but also as reference planes. The general setup can be seen in Figure 3.10, and shows the seven detectors with a spacing of 2.5 cm between each other.

### 3 ToT-Measurement with Digital Oversampling

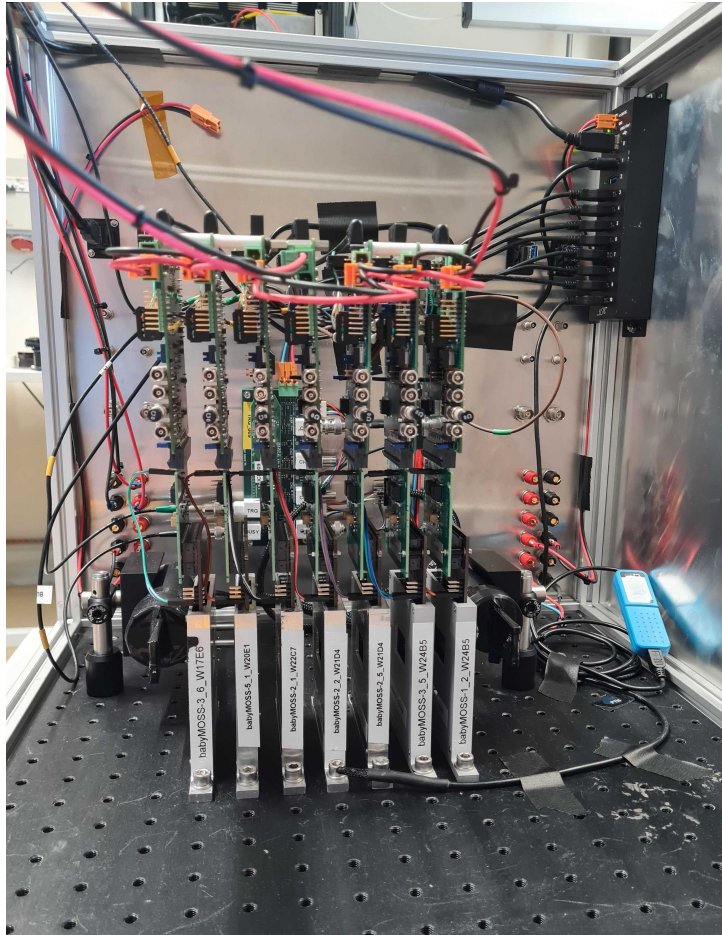


Figure 3.10: A picture of the seven BabyMOSS sensors (one DUT and six reference detectors) and the two scintillators that make up the beam telescope.

Additionally, a scintillator coupled to a photomultiplier is placed in front of the detector planes as well as behind it. These, in combination with a dedicated trigger board, are used to trigger all the sensors when a particle is detected and are essential for measuring the detection efficiency. All the components are placed in a metal box, shielding it from external light sources, and a temperature sensor is used to monitor the ambient temperature during the measurement.

The test beam itself was conducted by a group of seven people from various institutes at the Proton Synchrotron (PS) at CERN at the beamline T10, as seen in Figure 3.11. Acting as a pre-accelerator, the PS delivers beams not only to experiments but also to the Super Proton Synchrotron (SPS), which further accelerates particles before sending them to the Large Hadron Collider (LHC). For our setup, the beam delivered pions with an energy of approximately 10 GeV with around 1-2 spills per minute.

### 3 ToT-Measurement with Digital Oversampling

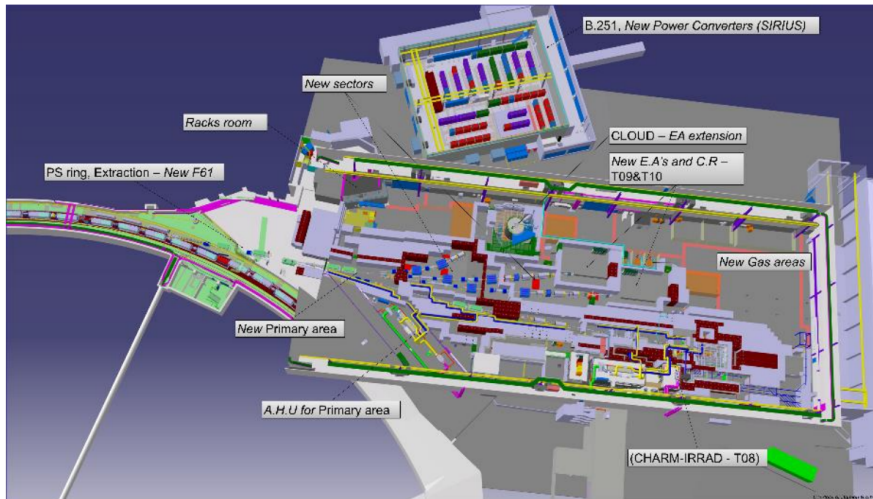


Figure 3.11: A map of the PS testing facility and the different beamlines used for test beams. [38]

The fully assembled telescope placed in the experimental hall is shown in Figure 3.12. The beam was used parasitically, meaning it was stationed behind another test setup to which the telescope had to be aligned carefully. Additionally, two power supplies are used for power distribution, together with a remotely accessible PC, which is used for data acquisition and general operation of the telescope.



Figure 3.12: A picture of the assembled telescope in the experimental hall.

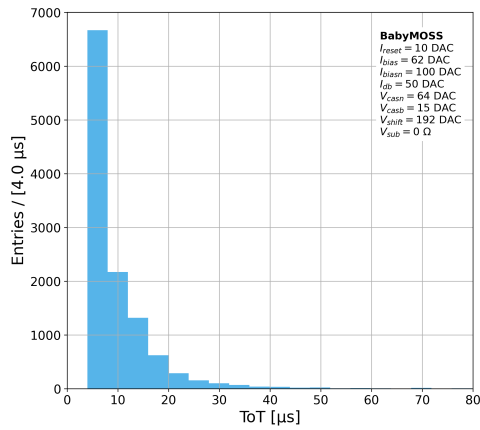
### 3 ToT-Measurement with Digital Oversampling

The plan for the test beam was to commission and demonstrate the first telescope with multiple BabyMOSS at CERN. For this purpose, the DUT was operated with and without back-bias voltage and scanning through different  $V_{\text{CASB}}$  values, essentially changing the threshold of the sensor. This was performed for both half-units and all regions of the DUT separately while keeping the other regions at the suggested nominal settings. This makes it possible to measure key properties of the detector, such as the detection efficiency, cluster size, and spatial resolution as a function of  $V_{\text{CASB}}$ . Furthermore, in phases without beam, threshold and fake-hit rate scans were performed so that the  $V_{\text{CASB}}$  values can be translated into threshold values. From this, the operational margin of the sensor is determined. The operational margin defines the range for which parameter settings the sensor can be used, given the requirements set by the final experiment. In the case of the ITS3 upgrade, the requirements are detection efficiency above 99% and a fake-hit rate of less than  $10^{-6} - 10^{-7}$  (hits/pixel/event) [39].

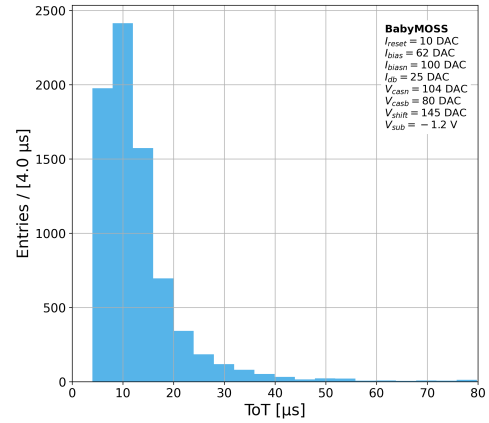
During the test beam, all the planned measurements could be performed so that additional time was available for other measurements. Therefore, several ToT scans were conducted using the oversampling method for all seven detectors to observe the ToT response of the BabyMOSS in a beam environment. In total, data was taken for four different sensor settings. The first scan was performed using the default settings without applying back-bias voltage and is shown for the DUT in Figure 3.13 (a). A prominent peak is observed at the first bin value, together with a fast-declining tail. In order to minimize noise contributions and to get an estimate of the signal shape, a second scan was done using a higher threshold value by setting  $V_{\text{CASB}} = 5 \text{ DAC}$ . This can be seen in Figure 3.13 (b), in which the first bin count decreased, and the spectrum resembles a Landau distribution.

The Landau distribution [40] is often used in particle physics to describe the energy loss of charged particles passing through thin layers of material, such as those found in MAPS detectors. When a charged particle, like a proton or pion, traverses a silicon detector, it ionizes the material, producing a cascade of electrons. The amount of energy deposited varies due to statistical fluctuations in the number and size of collisions following a Landau distribution. This distribution is characterized by a peak, or most probable value, and a long tail extending toward higher energy losses.

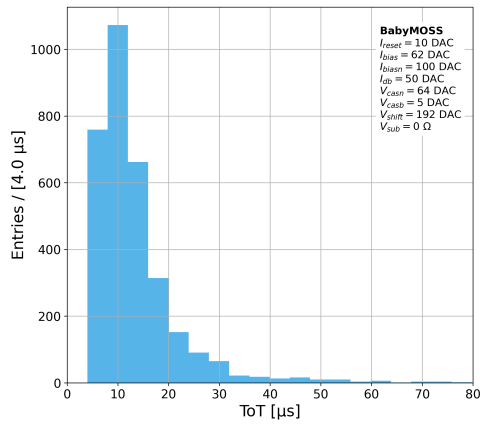
### 3 ToT-Measurement with Digital Oversampling



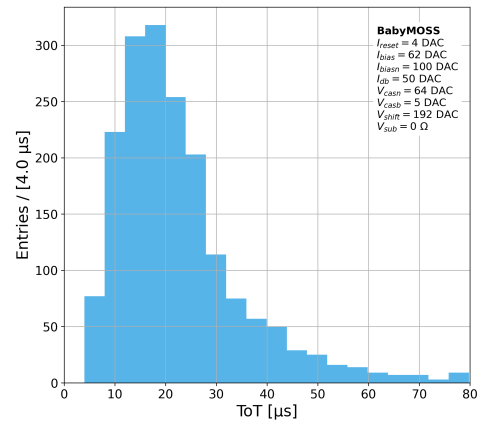
(a)  $I_{\text{Reset}} = 10 \text{ DAC} \mid V_{\text{Vcasb}} = 15 \text{ DAC}$



(b)  $I_{\text{Reset}} = 10 \text{ DAC} \mid V_{\text{Vcasb}} = 805 \text{ DAC}$



(c)  $I_{\text{Reset}} = 10 \text{ DAC} \mid V_{\text{Vcasb}} = 5 \text{ DAC}$



(d)  $I_{\text{Reset}} = 4 \text{ DAC} \mid V_{\text{Vcasb}} = 5 \text{ DAC}$

Figure 3.13: The ToT distributions of the various settings that were tested.

Additionally, for the DUT, a scan was performed applying a back-bias voltage of  $-1.2 \text{ V}$  as seen in Figure 3.13 (c). The  $V_{\text{CASB}}$  was set to 80 DAC, which should lead to a threshold similar to the scan without back-bias and  $V_{\text{CASB}} = 5 \text{ DAC}$ . Comparing these two measurements suggests that the applied back-bias voltage does not significantly affect the Time-over-Threshold response, as the overall shapes are almost identical, with a difference observed in the lowest bins, which could be due to slightly different threshold and noise levels at the different parameter values.

A last measurement was conducted setting  $I_{\text{RESET}}$  to 4 DAC, therefore extending the analog signal in the pixel and keeping  $V_{\text{CASB}}$  at 5 DAC. The resulting ToT distribution is shown in Figure 3.13 (d). The widened spectrum now clearly shows the features of a Landau distribution, with a peak (most probable value)

### 3 ToT-Measurement with Digital Oversampling

at around 16  $\mu\text{s}$ , followed by a long tail.

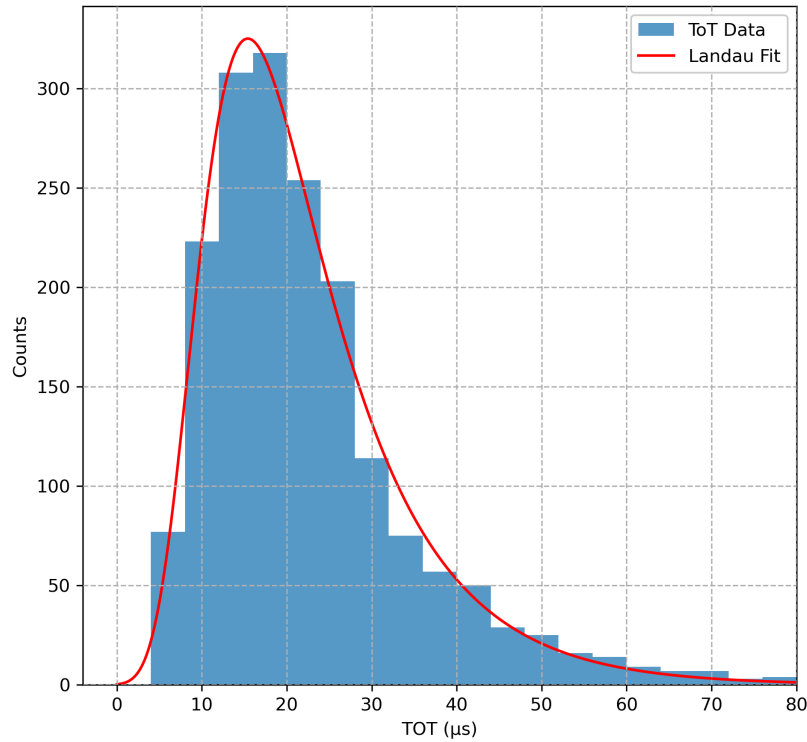


Figure 3.14: The ToT distribution for the DUT with  $I_{\text{RESET}} = 4 \text{ DAC}$  and  $V_{\text{CASB}} = 5 \text{ DAC}$ , fitted with a Landau distribution.

An example of a fitted Landau distribution to the DUT data is displayed in Figure 3.14. The extension towards a fit for all detectors is shown in Figure 3.15. Of the original seven BabyMOSS, only five of them are plotted since one detector did not record data and another one had a significant noise contribution and is, therefore, rejected in the ToT analysis. Each histogram is normalized to the highest bin count to compare the distribution shape rather than absolute values. Overall, the histograms and fits overlap and agree with one another, pointing to the fact that the ToT response across different BabyMOSS sensors is equivalent with little deviation. The slight differences between the spectra are most likely due to chip-to-chip variations of threshold and noise, which can alter the distribution, as no noisy pixels were masked during the scan or the analysis.

### 3 ToT-Measurement with Digital Oversampling

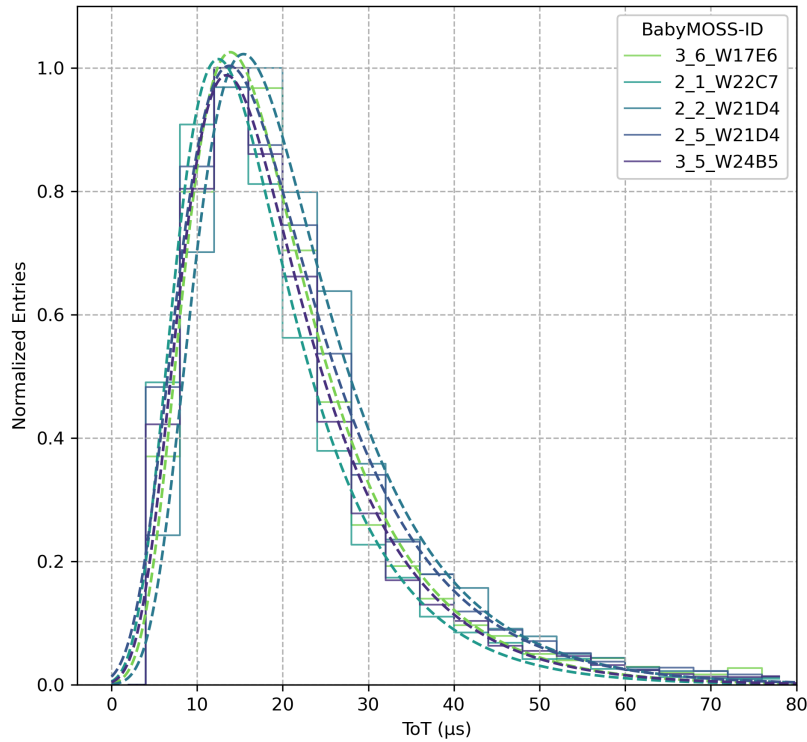


Figure 3.15: The ToT distributions of five detectors overlaid and normalized to the highest count, each fitted with a Landau distribution.

In order to study the ToT response and uniformity within the sensor matrix, one can divide each detector region, which is scanned into smaller subregions. This is shown in Figure 3.16. The five different 2D histograms each resemble one of the BabyMOSS. They show the measured region or pixel matrix, divided further into subregions in a grid structure of  $8 \times 8$ . The mean of the ToT distribution within the subregions is calculated and indicated by the colorbar. To exclude subregions with very few statistics, only subregions that have a higher count than 20 are shown. In general, the mean ToT values vary from roughly 13 to 22  $\mu\text{s}$ . Given the low statistics of almost no subregions with 100 counts or higher, this is to be expected. However, the values are uniformly and ‘randomly’ distributed, and no significant change or tendency within the matrix is observed for either of the detectors.

### 3 ToT-Measurement with Digital Oversampling

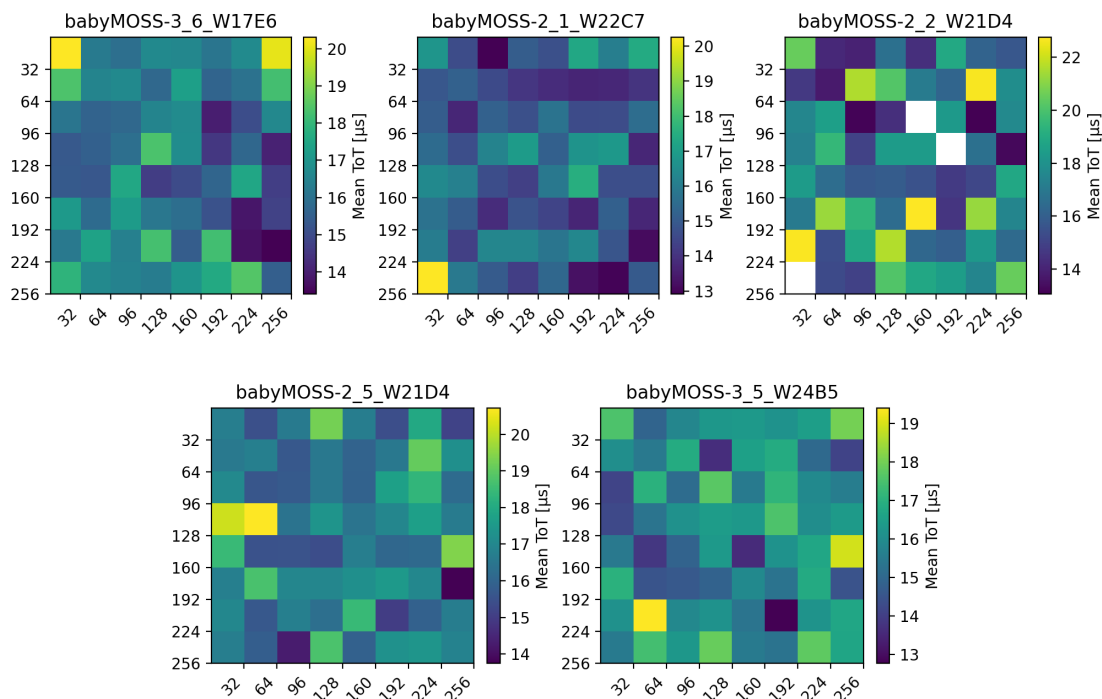


Figure 3.16: The five different 2D histograms correspond to the studied pixel matrix of five different BabyMOSS detectors. The matrix is divided into several subregions in a grid structure of  $8 \times 8$ , and the mean ToT value is plotted for each subregion.

During the test beam, the ToT data was collected without external triggering, making it impractical to correlate data from multiple detector planes with global tracks or events. However, this information would be beneficial in providing insight into the performance of a possible multi-layer tracker with ToT measuring capabilities.

Typically, the energy resolution achievable by a detector measuring ionization is influenced by the volume of material available for ionization. Since the current MAPS detectors are manufactured with thicknesses of as small as  $50 \mu\text{m}$  or lower, and an even thinner epitaxial layer that corresponds to the active volume. A multi-layer setup would, therefore, improve the energy resolution as it principally increases the active volume of the detector by the number of layers, not considering effects from thresholds, etc. Future experiments, such as ALICE3, could make use of this technique as it will have several detector layers within the barrel and the discs, with up to 10-11 hits per track possible.

### 3 ToT-Measurement with Digital Oversampling

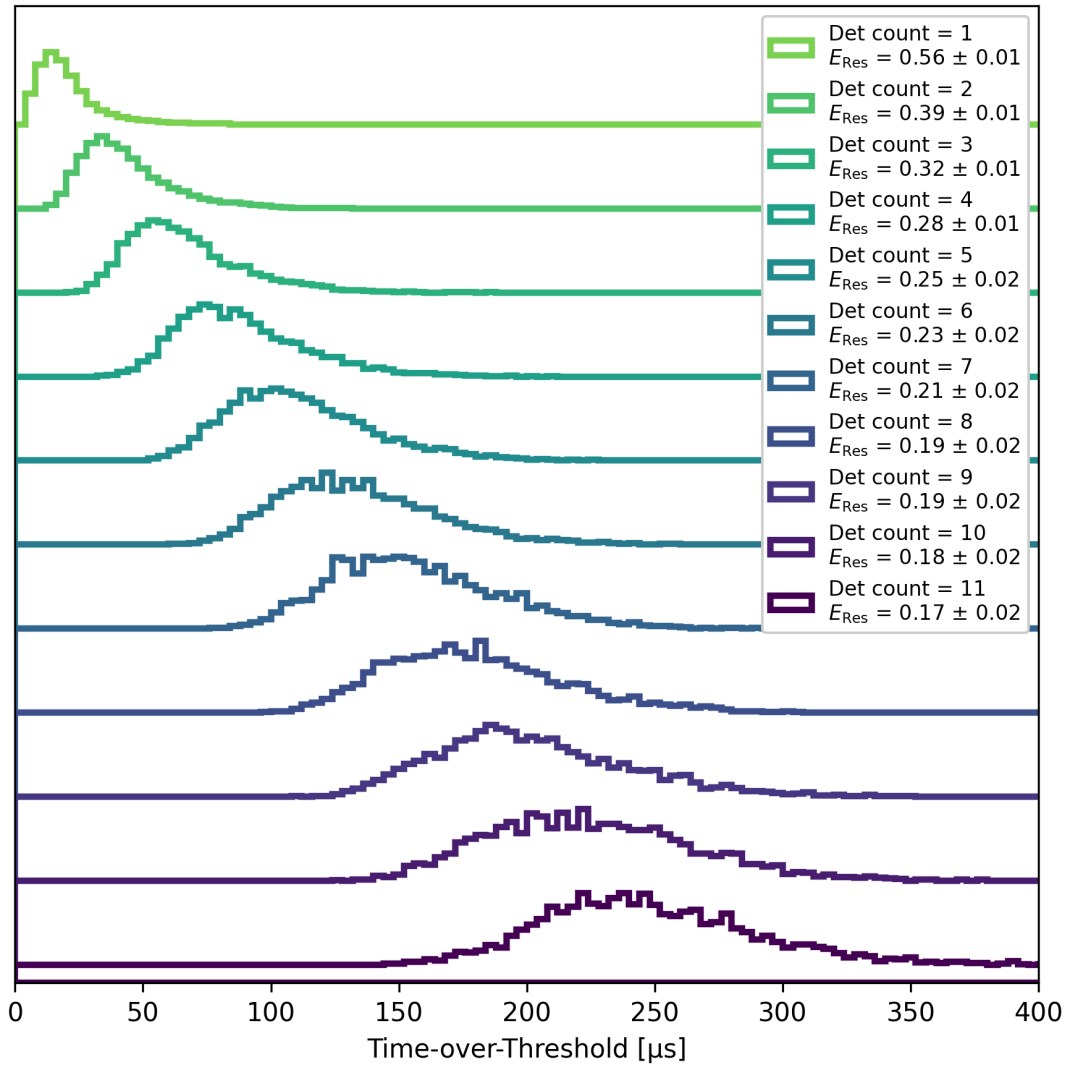


Figure 3.17: The summed-up ToT values displayed in the different histograms, each one corresponding to a different number of detectors taken into account.

A simplification was made to replicate this with the measured test beam data, even without tracking information. First, all data from the five detectors is combined into one list. Since all the hits are uncorrelated and statistically equally distributed, one can randomly sum up the number of  $n$  values from the data list, depending on the number of detectors  $n$  that are being replicated. For each detector count, these summed values can be plotted in histograms, as shown in Figure 3.17. For the ‘raw’ data with one detector plane, the observed distribution again resembles a Landau. Moving towards a higher detector count with continuously more hits summed up, the distribution begins to approach the shape of a Gaussian function. The energy resolution of the spectrum for

### 3 ToT-Measurement with Digital Oversampling

each plane is estimated by dividing the standard deviation of the distribution by the mean and is given in Table 3.1.

Detector count	1	2	3	4	5	6
$E_{\text{Res}}$	$(56 \pm 1) \%$	$(39 \pm 1) \%$	$(32 \pm 1) \%$	$(28 \pm 1) \%$	$(25 \pm 2) \%$	$(23 \pm 2) \%$

Detector count	7	8	9	10	11
$E_{\text{Res}}$	$(21 \pm 2) \%$	$(19 \pm 2) \%$	$(19 \pm 2) \%$	$(18 \pm 2) \%$	$(17 \pm 2) \%$

Table 3.1: The energy resolutions extracted from the summed ToT distributions for the different detector counts.

As expected, the energy resolution decreases with an increasing number of detectors. There is a drastic improvement in resolution after the first couple of layers, roughly halved after four layers in comparison to one detector, and a flattening towards the higher number of planes.

# 4 Impact and Feasibility of Amplitude Measurement for Pixel Detectors

## 4.1 State-of-the-Art PID

Particle Identification (PID) is a crucial tool used in high-energy physics experiments. It enables scientists to distinguish particles from one another, which is essential for tracking, reconstruction, and physics analyses. PID can be performed using various methods. One common method is using Time-of-Flight (TOF) detectors, which measure the time it takes for a particle to cross a certain distance. Since particles with different masses but similar momentum will travel at different velocities, this time measurement can be used to differentiate between particles. Another approach is to utilize RICH detectors, which identify particles by measuring the intensity and angle of the emitted characteristic cone produced when they enter the medium at a faster speed than the speed of light in that medium. Combined with momentum measurements using, for example, the bending radius within an applied magnetic field, this can be used to identify the particle species.

In addition, other methods like direct energy loss ( $dE/dx$ ) measurements are also employed. As particles pass through a material, they ionize the matter, and the magnitude of this energy loss is dependent on the particle charge and momentum. This energy loss is measured in various types of detectors, such as drift chambers and time projection chambers, and is used to identify different particles by comparing the measured  $dE/dx$  in combination with the Bethe-Bloch formula. Detectors such as Transition Radiation Detectors (TRD) can also be used for PID, where particles emit X-ray photons when passing through layers of materials with different refractive indices, allowing for the distinction of, for example, electrons from other particles.

However, tracking detectors, such as those based on silicon pixel sensors, typically do not directly perform PID. Their main function is to precisely measure the track of particles going through the detector, providing important information on the momentum and position but not directly identifying the type of particle.

It would still be advantageous to have a tracker that could deliver some level

of particle identification (PID), given that tracking detectors operate through the ionization process, which inherently offers information relevant to PID. One approach that utilizes this information is the use of cluster size in MAPS detectors, which has become an integral part of the main analysis pipeline for the Inner Tracking System (ITS2) of ALICE. Cluster size refers to the number of neighboring pixels that register a hit when a charged particle passes through the detector. The size of these clusters depends not only on the type of particle but also on its momentum and its position on the Bethe-Bloch curve. Particles that ionize more strongly, depending on where they fall on the Bethe-Bloch curve, will produce larger clusters, while those ionizing less will create smaller clusters. An example of such PID using cluster size (corrected for the angle using the cosine) information is shown in Figure 4.1, where protons are distinguished from pions at momenta of 0.4 - 0.6 GeV/c.

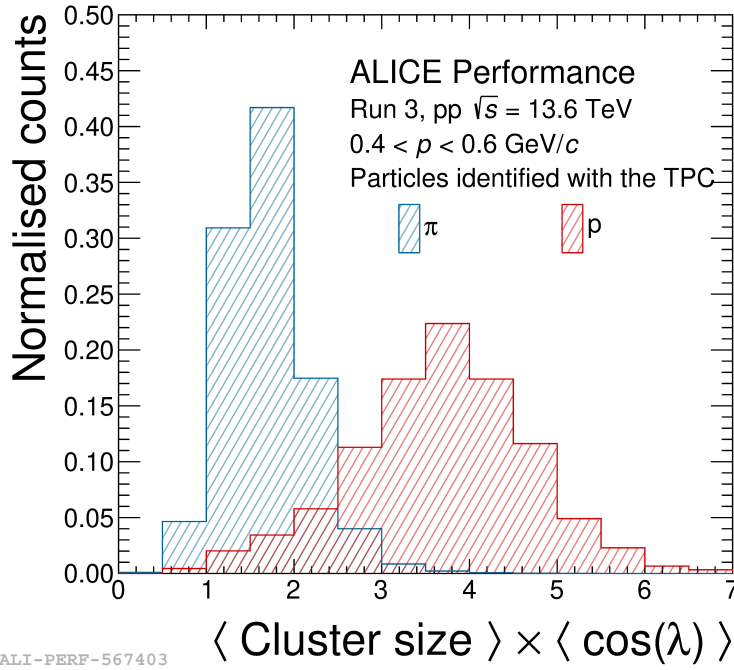


Figure 4.1: A performance plot from ITS2 using cluster size for PID to distinguish between protons and pions. [41]

With the new 65 nm CMOS imaging technology and different doping profiles within the pixel, however, the cluster size information is essentially lost. This is because it will primarily measure cluster size one and cannot be used to gain information on the energy deposition. Therefore, new approaches and advancements need to be developed to effectively use MAPS detectors for amplitude measurement purposes.

## 4.2 Example Use-Case for the ALICE3 Outer Tracker

As part of the upcoming Long Shutdown 4 (LS4) at CERN, the ALICE detector will not only undergo an upgrade but will be entirely replaced by a new detector system and configuration known as ALICE3 [42]. This successor is scheduled to begin data-taking for Run 5 in 2035. The new detector will be more compact, incorporating novel technologies that enable higher readout rates. A key physics goal of ALICE3 is to deepen our understanding of QCD and the QGP through heavy-ion collisions at even higher rates than currently. Figure 4.2 shows a schematic of one of the possible configurations.

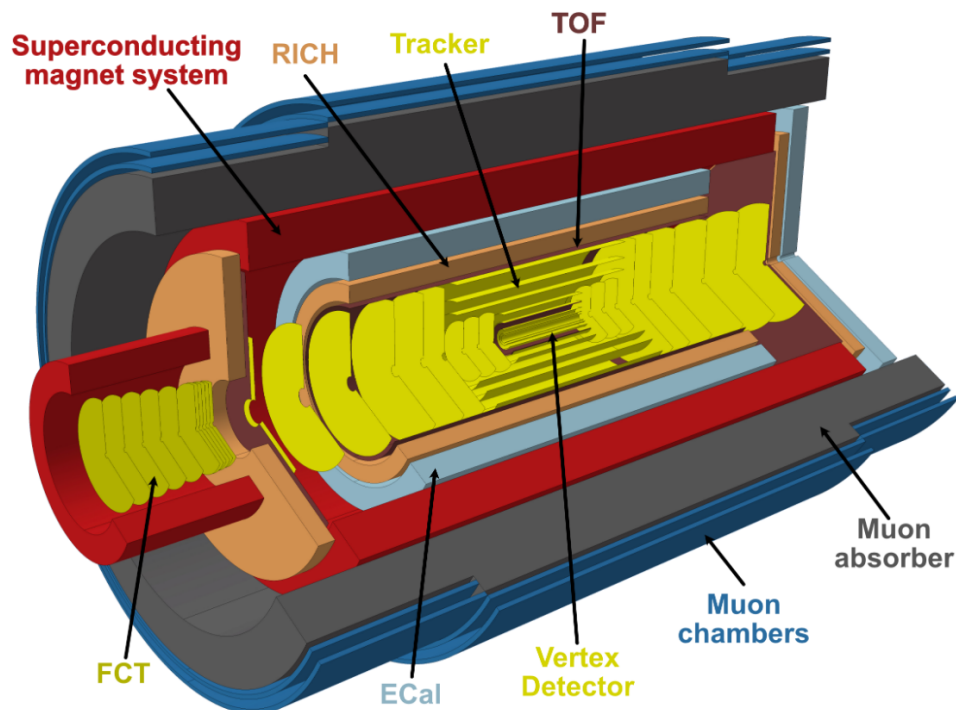


Figure 4.2: From the Letter Of Intent (LOI): A schematic of the possible detector and subsystem configurations for ALICE3. [42]

ALICE3 will feature a new, more compact superconducting magnet system with an increased magnetic field. Without the TPC, the PID will primarily be managed by RICH detectors in combination with two layers of TOF detectors. Additionally, there is an option to incorporate an Electromagnetic Calorimeter (ECal). A muon absorber and muon chambers will be integrated into the outer region of the detector, which will be responsible for tracking and identifying muons.

The innermost section will utilize silicon tracking detectors of MAPS, organized into the Inner and Outer Tracker (IT/OT) layers. In ALICE3, a significant advancement is the planned vertex detector, which will be integrated within

the beam pipe and designed to move closer to the particle beam and interaction point during data-taking. Compared to the existing ITS2 and the upcoming ITS3, ALICE3 will also feature discs on both sides of the barrels, as well as an increased number of sensors and pixels overall.

One question that arises is whether the new detector could be used for amplitude measurements in addition to tracking. This could have a significant impact on particle identification at low momenta and tracking, especially the seeding process, for example, using ACTS (A Common Tracking Software) [43]. Seeding in tracking involves the initial selection of hit points to estimate potential particle trajectories. This serves as the foundation for more detailed track reconstruction, typically using a small number of points to create an initial estimate of the particle track.

Considering the geometry of ALICE3 and the outer tracker, the maximum expected hits per track measured will be 10-11. Therefore, the concept of using the silicon trackers for amplitude measurement and PID first has to be proved. In this thesis, the energy loss of various particles and momenta through layers of silicon is simulated using Geant4 [44] in order to estimate the capability of MAPS to separate different particles for PID.

### 4.3 Geant4 Simulation

Geant4 (Geometry and tracking) [44] is a software first developed at CERN and used to simulate particles passing through matter. It is a versatile tool for simulations, as one can build one's own world and detector geometry with a large variety of common particle types and physical interactions with matter. Geant4 is based on C++ and uses different modules to describe and run the simulation, including PhysicsList, DetectorConstruction, ActionInitialization, PrimaryGeneratorAction, EventAction, SteppingAction, and main. The PhysicsList describes the different interactions that are included and possible in the simulation. Most importantly, the StandardPhysics class is included, which handles the standard electromagnetic processes, as well as HadronElasticPhysics, StoppingPhysics, and IonPhysics.

The DetectorConstruction module is used to define the world in which the simulation takes place and builds the detectors with their specific properties within. In the scope of this thesis, the setup incorporates 11 detector layers to replicate the maximum number of hits possible in an ALICE3 track, with a spacing of 10 cm between them and oriented along the z-axis. The thickness of these silicon layers varied between 10 and 20  $\mu\text{m}$ . The surrounding of the detectors is chosen to be a vacuum.

The ActionInitialization is used to coordinate and execute the action modules. Using the PrimaryGeneratorAction, the particles can be created and simulated. A so-called particle gun generates the specified particle type, which can be

imported from a databank, the ParticleTable. Furthermore, the particle energy, origin, and direction can be defined. In these simulations, six different particles were investigated: protons, positrons, pions, kaons, deuterons, and helium-3 ( $^3\text{He}$ ). Only the positive type of each particle was used to compare the same side of the Bethe-Bloch curve, which is often shown as a function of momentum ( $p/z$ ). They were created at a distance of 10 cm to the first sensor layer and moved along the  $z$  direction. The EventAction module manages the start and end of each event, including the particle going through the simulation and passing through the detectors, as well as collecting and outputting the results of the interactions, in my case, the deposited energy in the layers. This is done in combination with the SteppingAction module. This module breaks the particle path up into smaller steps and provides access to the current state of the particle. It can be customized to execute different actions at each step, such as collecting data regarding the energy deposition within the silicon. This is implemented by checking if the interaction took place within the sensor volume and using the GetTotalEnergyDeposit class. Finally, the main module is responsible for the initialization and execution of all modules for the simulation and handles the inputs given by the macro file, in which simple parameters, such as the particle energy and type or the number of events, can be configured.

The first simulation involved incorporating only one layer of silicon and generating negative pions with a momentum of  $10\text{ GeV}/c$  in order to replicate the scenario of a single BabyMOSS sensor at a test beam. A comparison between the simulation and the test beam data with normalized counts is shown in Figure 4.3. The conversion of the energy deposition that Geant4 generates is handled by using the position of the  $^{55}\text{Fe}$  main peak at the same settings as a calibration point. As expected, the Geant4 simulation also leads to a Landau distribution for the energy loss, as it describes the statistical interaction of particles traversing through a (thin) material. A threshold was subsequently implemented by removing the energy deposition below a set threshold and subtracting the threshold value from the remaining events. The threshold value in the test beam is not exactly known but was estimated to be around 200 electrons for the settings used. The resulting distribution can be seen on the right plot in Figure 4.3. After applying the threshold correction, the two distributions are fully in agreement, considering that the threshold is not precisely known and that other effects in the sensor can introduce distortions to the Landau.

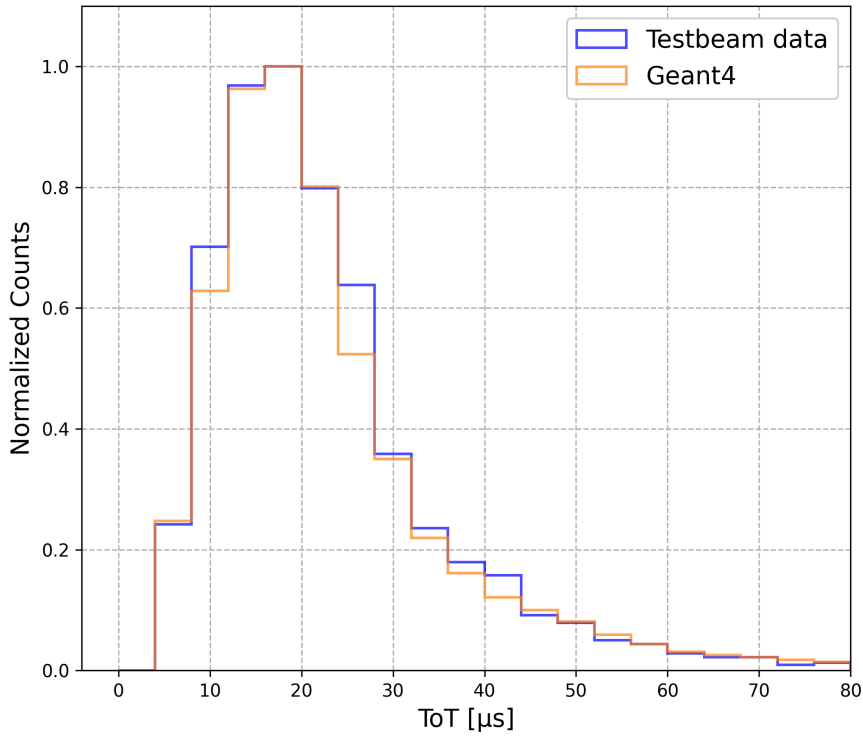


Figure 4.3: A comparison between the ToT distribution measured during the test beam campaign and the Geant4 simulation for one silicon layer with an implemented threshold to the simulated data of approximately  $200 e^-$ .

The second part of these studies involved simulating particles traversing through all 11 detector layers of  $10 \mu\text{m}$  thick silicon. In order to estimate the separation capability of MAPS detectors in such a scenario (e.g., ALICE3 outer tracker), several different particles are generated, and the energy deposition in each layer, as well as the total energy loss, is investigated. This is then repeated for different particle momenta to establish in which momentum regime a particle differentiation is feasible. The threshold is set in the analysis to approximately 100 electrons and the energy loss per layer binned before summing them up to the total energy deposit.

The results are displayed as a function of the average Time-over-Threshold (ToT) in Figure 4.4, plotted on a logarithmic scale and using a sampling and signal length similar to the test beam measurements. The average ToT is obtained by dividing the total energy loss by the number of layers. All particles can be distinguished at the lowest momentum of  $0.1 \text{ GeV}/c$ . As momentum increases, it becomes harder to differentiate between lighter particles. This occurs because of the characteristics of the Bethe-Bloch curve, where at momenta above the particle mass, it becomes a Minimum Ionizing Particle (MIP). Beyond the minimum point of the equation, the curve rises only slightly. Since different particle

#### 4 Impact and Feasibility of Amplitude Measurement for Pixel Detectors

types have similar energy losses when they become MIPs, their distributions will start to overlap as momentum increases, as is the case for positrons and pions at 0.3 GeV/c.

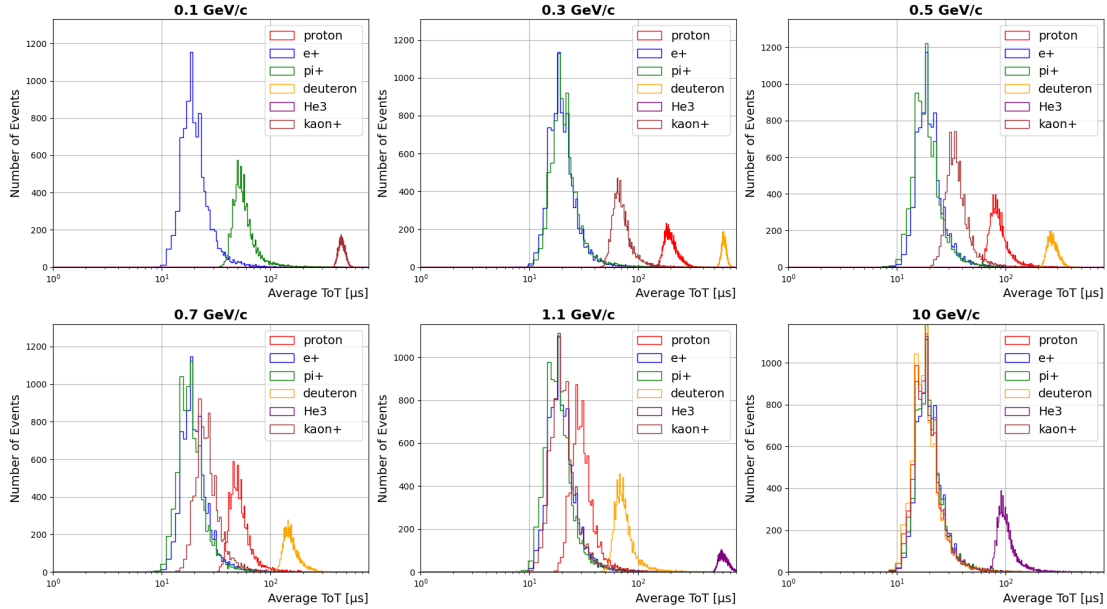


Figure 4.4: Geant4 simulations of various particles passing through 11 layers of 10  $\mu\text{m}$  thick silicon, showing the energy deposition converted to ToT at different momenta.

Since the thickness of the layers is set to 10  $\mu\text{m}$  and the particles traverse through the sensor directly orthogonal, the assumption is made that the particle will not pass through the layers at an angle. Because this does not always hold true and different incident angles are possible, another simulation is conducted, increasing the thickness to 20  $\mu\text{m}$ . This aims to replicate an inclined path and could possibly increase the energy resolution as the particle passes more detector material, depositing more energy. As expected, it was observed that the energy deposition roughly doubles with twice the amount of silicon.

An important aspect to consider in real experiments is the signal length. An extensively long ToT will cause issues at high pixel occupancies. In such a case, the signal would not have enough time to drop back below the threshold. It was, therefore, also of interest to study how a shortened signal length affects the simulated average ToT. An example of a roughly 4.5 times shorter signal is shown in Figure 4.5. Additionally, the sampling period was changed to 500 ns, which is an ambitious but reasonable value for future experiments. As a result, the average ToT decreases significantly about a factor of 4-5, and for example, protons already have an average ToT value below 100  $\mu\text{s}$  at a momentum of 0.3 GeV/c.

## 4 Impact and Feasibility of Amplitude Measurement for Pixel Detectors

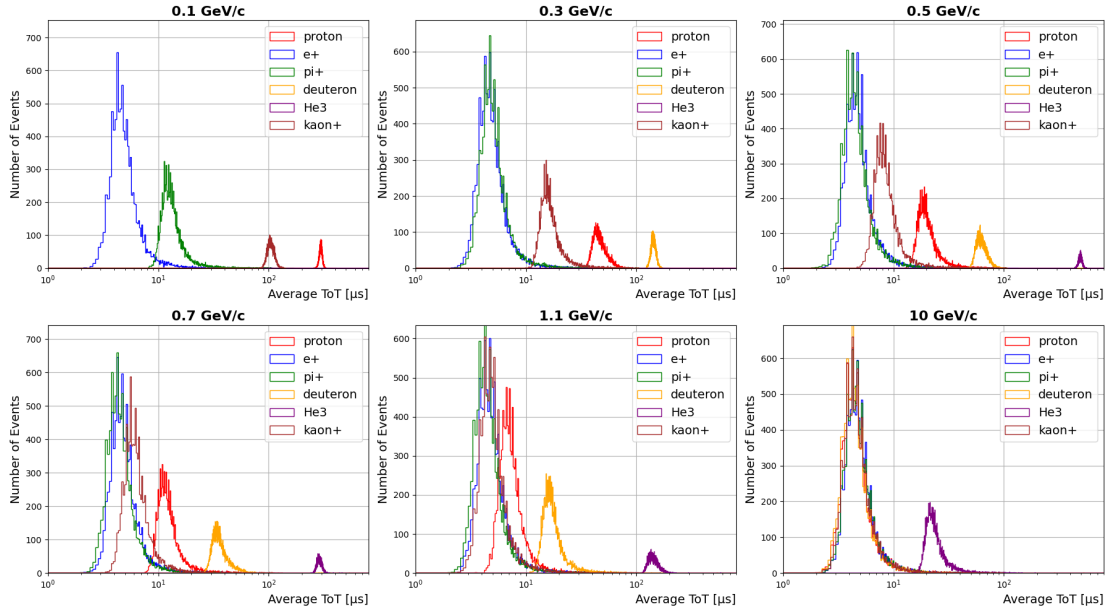


Figure 4.5: Geant4 simulations of various particles passing through 11 layers of 10  $\mu\text{m}$  thick silicon with a shortened signal length and a sampling period of 500 ns.

A crucial aspect of particle identification is the separation power, a quantitative measure that can be used to make statements about the ability of particles to be distinguished from one another. The formula that is used to calculate it is given by

$$SP = \frac{|\mu_A - \mu_B|}{\sqrt{\frac{\sigma_A^2 + \sigma_B^2}{2}}}, \quad (4.1)$$

with  $\mu$  the mean,  $\sigma$  the standard deviation, and A and B being the particles that are being studied. Only the three lightest particles were investigated since these make up the majority of the particles. The separation power for the particle pairs pion-kaon, pion-proton, and kaon-proton are displayed in Figure 4.6, varying the silicon thickness, as well as the number of layers. For all pairs in general, an improvement is observed towards the thicker sensor and a higher number of layers. For the pion-kaon and kaon-proton case, a separation power of 1 can be achieved up to 0.5 GeV/c and 0.7 GeV/c, respectively. This value seems to be even higher for the pion-proton case, and a separation of power of 3 can be achieved up to 0.5 GeV/c.

## 4 Impact and Feasibility of Amplitude Measurement for Pixel Detectors

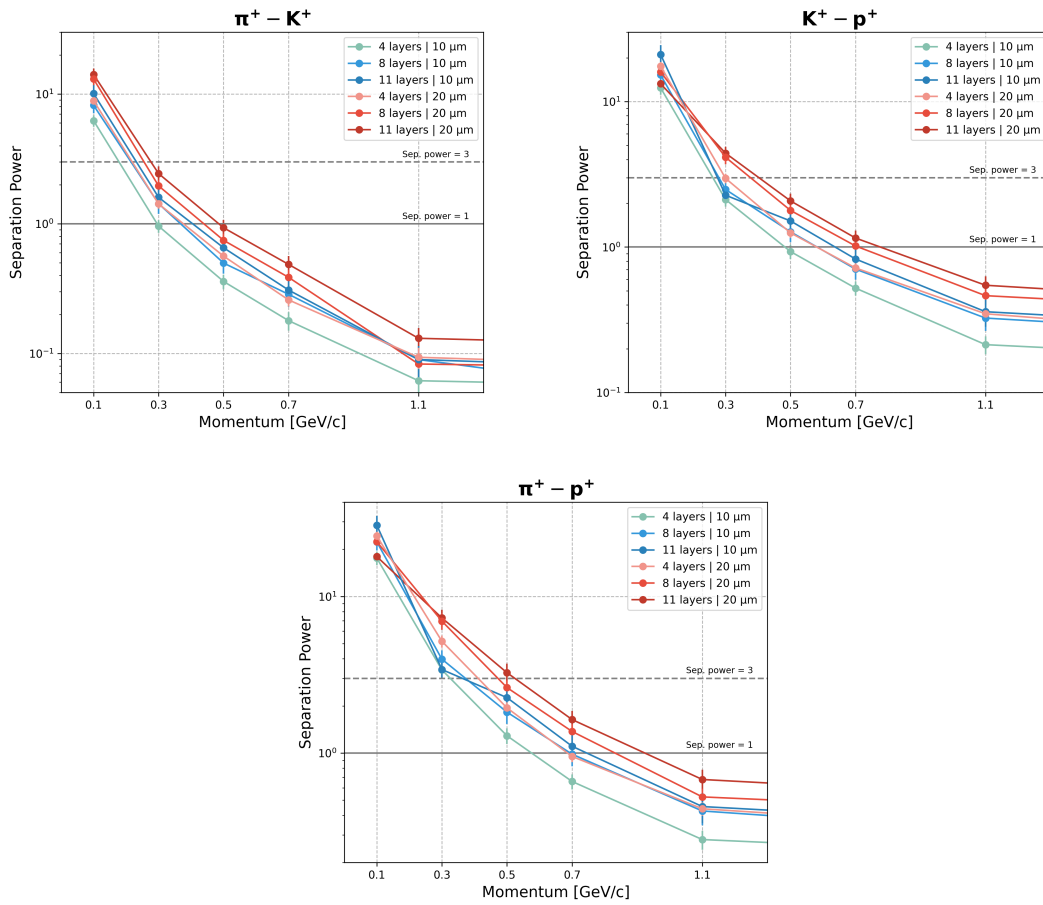


Figure 4.6: The separation power for pion-kaon, kaon-proton, and pion-proton, as a function of the momentum for a different number of layers and silicon thickness.

This suggests that using multiple MAPS detectors is a feasible approach to distinguish between particles and that PID is possible in the lower momentum range ( $< 1 \text{ GeV}/c$ ).

## 5 Conclusion and Outlook

In this thesis, different methods for amplitude measurement with MAPS detectors were explored, involving the BabyMOSS and the DPTS sensors. In addition, Geant4 simulations were carried out to study the feasibility of using Time-over-Threshold information in future experiments like ALICE3.

For the first part of these studies, the DPTS sensor was investigated. The chip utilizes signals in which the hit position and the ToT are time-encoded. An FPGA-based readout was implemented using the TRB3Sc board, which integrates TDC-in-FPGA technology with a timing precision of several picoseconds. The performance of this readout system was evaluated and compared to the original readout method via picoscope. The test involved several criteria and scans, including signal decoding, threshold scans, ToT calibrations, and source measurements with an X-ray source. Overall, the FPGA readout performed almost equivalent to the picoscope readout in all aspects. Some issues arise during the decoding, which affects, for example, the threshold analysis. Furthermore, the energy resolution of the main peak in the iron spectrum is slightly worse, and the  $K_\alpha$ -peak can not be distinguished. Nonetheless, the results meet the expectations for the FPGA readout version that is currently implemented. With additional updates to automate the readout process, speed up data acquisition, and improve the analysis, a fully functional and capable readout system with equivalent performance should be achievable in the future. Most importantly, the demonstrated readout could also be used for larger sensors that implement similar encoded ToT information, such as the MOST detector [39], and for future next-generation detectors with amplitude measurement properties.

The second part of these studies investigated ToT measurements using the digital oversampling method with BabyMOSS. Source measurements with an X-ray source served as a starting point to test how different parameters affect the ToT distribution. Changing front-end parameters such as  $I_{\text{Reset}}$ , the signal length could be extended, which helps to pronounce the main peak. By varying the value of  $V_{\text{Casb}}$ , the threshold within the pixels was modified, which also slightly affected the ToT duration. In addition, a Gaussian was fitted to the main peak of the iron spectrum to estimate the peak position. Combining these methods, the analog signal shape of the BabyMOSS was probed by observing how the ToT distribution shifts as a function of the threshold and for different  $I_{\text{Reset}}$  values. The result shows that the signal in the probed regime behaves linearly and that the corresponding slope gets steeper with decreasing  $I_{\text{Reset}}$ .

## 5 Conclusion and Outlook

This is in agreement with the observations made with the monitor pixel from the DPTS sensor, which possesses a similar front end. Moreover, the pixel-by-pixel ToT response was investigated, and an attempt was made to calibrate for these variations. Although the final result of the calibration was partially successful, it did not lead to a significant improvement in energy resolution. This suggests that further modifications are necessary to obtain a beneficial pixel-by-pixel ToT calibration through, for example, increased statistics and additional calibration points of known energy.

Apart from source measurements, a test beam was also conducted with a telescope, recreating a more realistic environment as in real high-energy physics experiments. ToT scans were performed with seven BabyMOSS sensors, while in the end, five detectors recorded functional data with low enough noise contributions. The uniformity of the ToT response across the pixels was measured, and the typical for a 10 GeV/c pion beam expected Landau distribution was observed. A multi-layer detector setup was replicated by combining all the collected data and summing up randomly selected values. Considering ToT information from 11 detector layers, the results suggest that a significant improvement in energy resolution can be achieved.

The last part of the amplitude measurement studies is simulations using Geant4. The first simulation was done with one layer of 10  $\mu\text{m}$  thick silicon and 10 GeV/c negative pions to compare the energy deposition to the measured test beam data with BabyMOSS. With the implementation of a threshold, the comparison shows full agreement. The central part of the simulations was to introduce 11 layers of silicon and to investigate the energy deposited by different particle species, especially at lower momenta. The output, converted into ToT using values estimated from source measurements, was used to assess the PID capability by calculating the separation power between different particles. It was demonstrated that for a higher number of layers and an increased thickness, the separation power can be improved to up to 1 and higher at 0.5 GeV/c for the pion-kaon and kaon-proton case, and up to 1 for the pion-proton pair for momenta of 0.7 GeV/c and above.

In conclusion, the presented studies show that the employment of Time-over-Threshold methods to obtain information on energy deposition with MAPS is feasible and should be followed in the future. Considering the upcoming ALICE3 project and the general advancements in the MAPS community, additional R&D efforts should be made to investigate the technical requirements and possibilities of amplitude measurements in future experiments. One such idea is illustrated in Figure 5.1.

## 5 Conclusion and Outlook

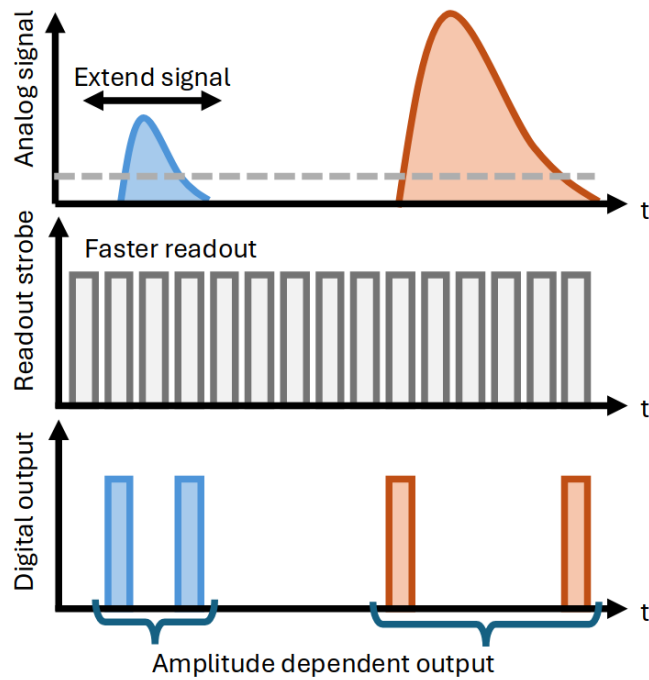


Figure 5.1: A sketch of a possible ToT implementation with digital oversampling for future sensors, with a 'minor' data increase compared to the current oversampling method.

Utilizing the digital oversampling method, one could design the chip and pixels in such a way that a signal is only sent out at the first sampled hit (rising edge) and the last sampled hit (falling edge). The time difference between the sent pulses could be measured and gives the Time-over-Threshold. This would dramatically decrease data output compared to the traditional oversampling, as the output is essentially only doubled with respect to the standard operation mode.

# Appendix

This section contains the additional simulation results for the parameter space that was investigated with the 11-layer setup.

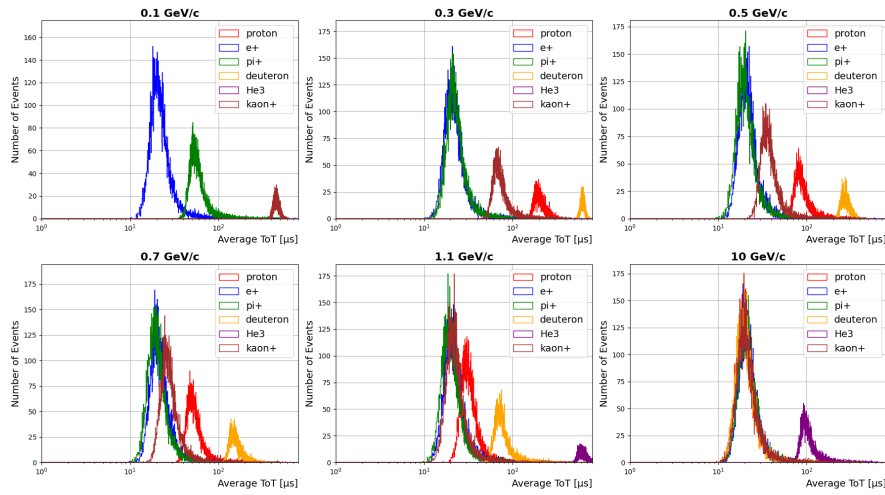


Figure 2: Geant4 simulations of various particles passing through 11 layers of 10  $\mu\text{m}$  thick silicon with a sampling period of 500 ns.

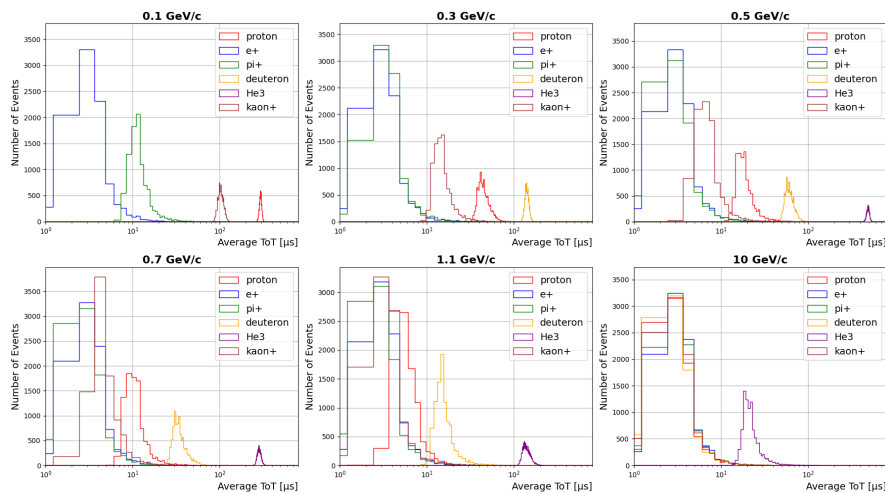


Figure 3: Geant4 simulations of various particles passing through 11 layers of 10  $\mu\text{m}$  thick silicon with a shortened signal length and a sampling period of 4  $\mu\text{s}$ .

## 5 Conclusion and Outlook

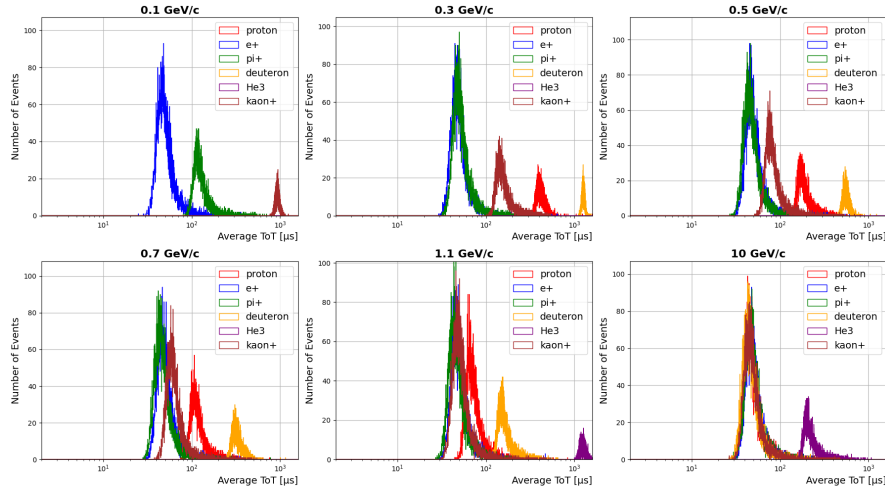


Figure 4: Geant4 simulations of various particles passing through 11 layers of 20  $\mu\text{m}$  thick silicon with a sampling period of 500 ns.

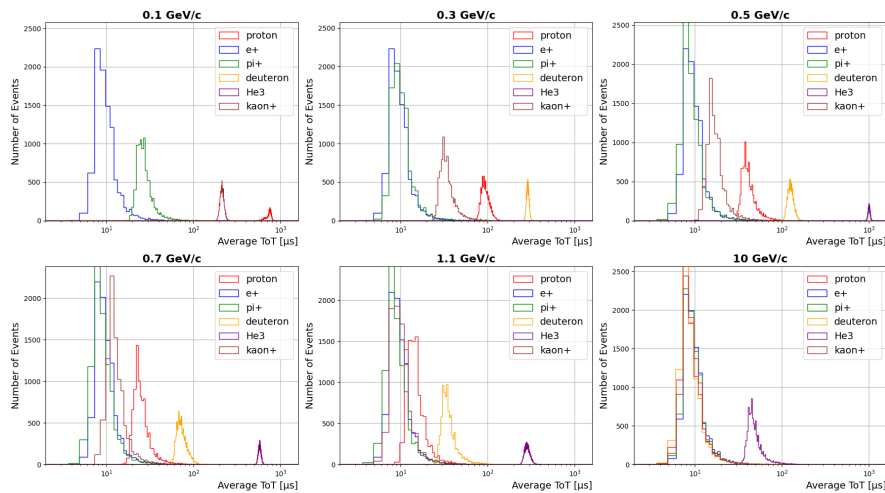


Figure 5: Geant4 simulations of various particles passing through 11 layers of 20  $\mu\text{m}$  thick silicon with a shortened signal length and a sampling period of 4  $\mu\text{s}$ .

## 5 Conclusion and Outlook

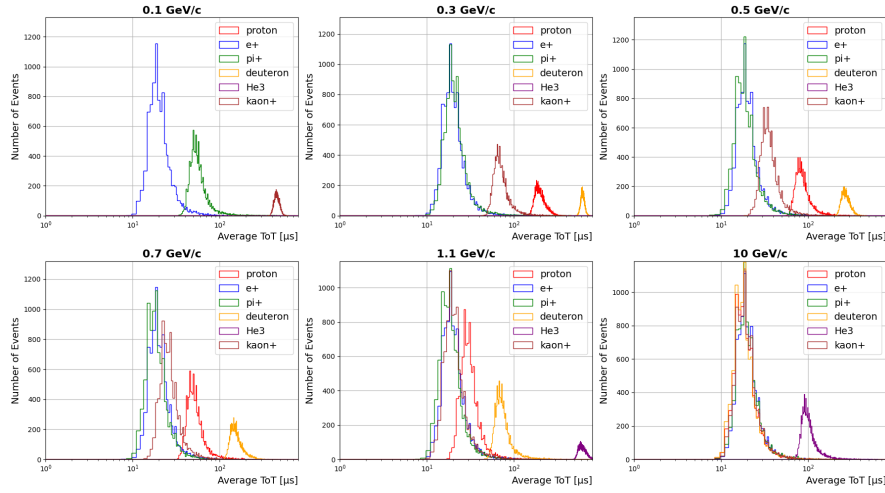


Figure 6: Geant4 simulations of various particles passing through 11 layers of  $20\ \mu\text{m}$  thick silicon with a sampling period of  $4\ \mu\text{s}$ .

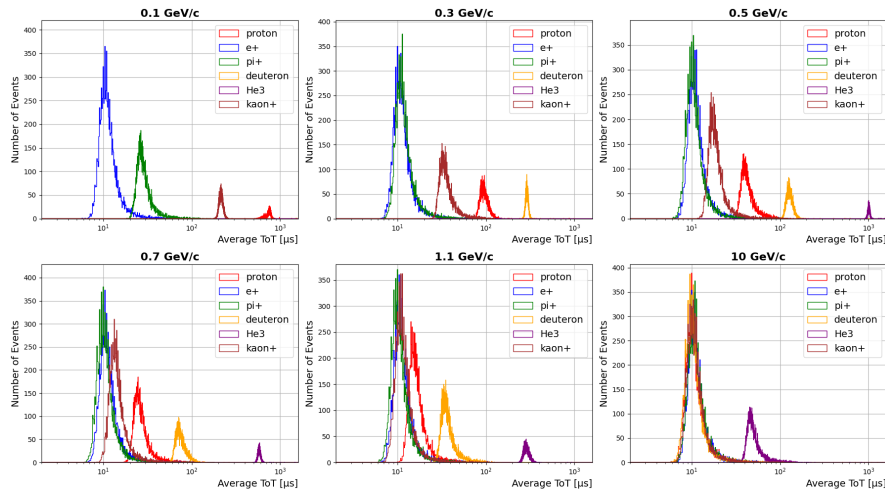


Figure 7: Geant4 simulations of various particles passing through 11 layers of  $20\ \mu\text{m}$  thick silicon with shortened signal length and a sampling period of  $500\ \text{ns}$ .

# Acknowledgments

First of all, I want to thank Prof. Laura Fabbietti for letting me work and exercise research in her friendly group. I would especially like to thank my supervisor, Berkin Ulukutlu, for the help and support during this year and the master's thesis, as well as for the countless hours of having fun working together. I would also like to express gratitude to Dr. Roman Gernhäuser for all the expertise and help during my research. Furthermore, I would like to thank the other members of the MAPSCrew, including Lena Kirchner, Dr. Laszlo Varga, Alexander Musta, Jan Egger, Christopher Ehrich, and others, for their advice and company in the lab, the office, or at conferences. I would also like to thank Dr. Michael Böhmer. The DPTS FPGA project would not have been possible without his expertise and effort. I also want to express thanks to all the other people in the MAPS community who gave advice and used their time to help with the projects. Finally, I want to thank my family and friends for always encouraging and motivating me.

# List of Figures

1.1	Left: Aerial view of the LHC accelerator complex at CERN in Geneva, Switzerland [4]. Right: A picture of the tracks that were captured using a bubble chamber, which led to the discovery of the Z boson and the associated evidence for the weak neutral current [5]. . . . .	1
1.2	A schematic layout of the ALICE experiment and the present subdetectors. [12] . . . . .	3
1.3	Working principle and schematic cross-section of a MAPS pixel. [20] . . . . .	4
1.4	Left: The various contributions to the material budget with the current ITS2 geometry [20]. Right: A schematic of the outer and the inner barrel of the ITS2 in the stave configuration [23]. . . . .	5
1.5	Left: A schematic of the two ITS3 half barrels with cylindrical geometry supported by carbon foam. Right: The pointing resolution of the ITS2 in comparison to the expected performance of the ITS3 upgrade as a function of the transverse momentum [23].	6
1.6	The pixel cross-section of the modified with gap process and a photo of the DPTS under a microscope [26]. . . . .	7
1.7	DPTS in-pixel front end, used for amplification, reset, and discrimination. [26] . . . . .	7
1.8	An example of how reticles are combined to form single sensors of a larger scale and active area. [28] . . . . .	8
1.9	The MOSS detector with ten stitched RSUs, which are each divided into top and bottom half-units with four different regions. [28] . . . . .	9
1.10	A close-up of the BabyMOSS sensor under the microscope, with all eight regions distinguishable. . . . .	10
2.1	A depiction of the pixel position- and the Time-over-Threshold encoding, involving two pulse trains and four pulses in total [26].	11
2.2	A sketch demonstrating how the ToT (Time-over-Threshold) of an analog signal is measured. . . . .	12
2.3	Different waveforms measured with the picoscope, demonstrating the difference of PID and GID for various pixels. . . . .	12
2.4	The pattern of the PID layout and the implementation of the column injection to the single digital output line. . . . .	13

*List of Figures*

2.5	Left: The setup for the DPTS measurements using the picoscope as a readout. Right: A picture of the FPGA-based readout using the TRB3Sc board. . . . .	14
2.6	The PID and GID are plotted after pulsing each pixel 100 times and assigning a center of gravity. . . . .	14
2.7	An S-curve outlining the threshold and noise of the pixel matrix.	15
2.8	The Time-over-Threshold (ToT) as a function of the injected voltage $V_H$ , including an example calibration curve for two pixels. . . . .	16
2.9	The measured $^{55}\text{Fe}$ energy spectrum, both before and after applying the ToT calibration. . . . .	17
2.10	A picture of the TRB3Sc with implemented TDC-in-FPGA technology. . . . .	19
2.11	An example of a Tapped Delay Line. [34] . . . . .	20
2.12	A sketch of the TDC implementation and the flip-flop logic used to decode the DPTS signals. . . . .	20
2.13	The measured calibration time as a function of the bin width for the three TDCs. . . . .	21
2.14	The decoding of the DPTS signals, obtained using the FPGA-based readout. It shows the measured PID and GID, as well as the center of gravity for each pixel. . . . .	23
2.15	Left: The S-curve obtained by performing a threshold scan for four rows with the FPGA-based readout. Right: The threshold distribution of the pixels fitted with a Gaussian. . . . .	23
2.16	The ToT response as a function of the injection voltage $V_H$ measured with the FPGA-based readout, including a linear fit for a pixel (5,5). . . . .	24
2.17	A comparison between the picoscope and the FPGA-based readout between the calibrated and uncalibrated $^{55}\text{Fe}$ -spectra. . . . .	26
2.18	A comparison between the picoscope and the FPGA-based readout between the energy resolution of the calibrated $^{55}\text{Fe}$ -spectra. . . . .	27
3.1	An example of how different signals are sampled exactly once, using an appropriate sampling period. . . . .	30
3.2	An illustration demonstrating how oversampling is used to measure ToT and distinguish signals of varying shapes. [36] . . . . .	31
3.3	An energy loss measurement performed with ALICE using the oversampling method with ALPIDE chips. [36] . . . . .	32
3.4	A picture of the BabyMOSS setup used for testing the sensor and performing source measurements. . . . .	33
3.5	Energy spectra obtained with an iron source using different settings, thereby changing the signal length and threshold. . . . .	34

*List of Figures*

3.6	The ToT distribution with a Gaussian fitted to the main peak of the spectrum. . . . .	35
3.7	The measured threshold as a function of the main peak position, plotted for different values of $I_{\text{RESET}}$ . . . . .	36
3.8	The mean ToT distribution for various pixels to demonstrate the pixel-to-pixel variation, fitted with a Gaussian. . . . .	36
3.9	Left: The pixel-by-pixel calibrated $^{55}\text{Fe}$ -spectrum in terms of deposited charge with a Gaussian fitted to the main peak. Right: The ToT distribution of all pixels for the performed source scan used for calibration. . . . .	37
3.10	A picture of the seven BabyMOSS sensors (one DUT and six reference detectors) and the two scintillators that make up the beam telescope. . . . .	39
3.11	A map of the PS testing facility and the different beamlines used for test beams. [38] . . . . .	40
3.12	A picture of the assembled telescope in the experimental hall. . .	40
3.13	The ToT distributions of the various settings that were tested. . .	42
3.14	The ToT distribution for the DUT with $I_{\text{RESET}} = 4\text{DAC}$ and $V_{\text{CASB}} = 5\text{DAC}$ , fitted with a Landau distribution. . . . .	43
3.15	The ToT distributions of five detectors overlaid and normalized to the highest count, each fitted with a Landau distribution. . . .	44
3.16	The five different 2D histograms correspond to the studied pixel matrix of five different BabyMOSS detectors. The matrix is divided into several subregions in a grid structure of $8 \times 8$ , and the mean ToT value is plotted for each subregion. . . . .	45
3.17	The summed-up ToT values displayed in the different histograms, each one corresponding to a different number of detectors taken into account. . . . .	46
4.1	A performance plot from ITS2 using cluster size for PID to distinguish between protons and pions. [41] . . . . .	49
4.2	From the Letter Of Intent (LOI): A schematic of the possible detector and subsystem configurations for ALICE3. [42] . . . . .	50
4.3	A comparison between the ToT distribution measured during the test beam campaign and the Geant4 simulation for one silicon layer with an implemented threshold to the simulated data of approximately $200\text{e}^-$ . . . . .	53
4.4	Geant4 simulations of various particles passing through 11 layers of $10\mu\text{m}$ thick silicon, showing the energy deposition converted to ToT at different momenta. . . . .	54

*List of Figures*

4.5	Geant4 simulations of various particles passing through 11 layers of 10 $\mu\text{m}$ thick silicon with a shortened signal length and a sampling period of 500 ns. . . . .	55
4.6	The separation power for pion-kaon, kaon-proton, and pion-proton, as a function of the momentum for a different number of layers and silicon thickness. . . . .	56
5.1	A sketch of a possible ToT implementation with digital oversampling for future sensors, with a 'minor' data increase compared to the current oversampling method. . . . .	59
2	Geant4 simulations of various particles passing through 11 layers of 10 $\mu\text{m}$ thick silicon with a sampling period of 500 ns. . . . .	60
3	Geant4 simulations of various particles passing through 11 layers of 10 $\mu\text{m}$ thick silicon with a shortened signal length and a sampling period of 4 $\mu\text{s}$ . . . . .	60
4	Geant4 simulations of various particles passing through 11 layers of 20 $\mu\text{m}$ thick silicon with a sampling period of 500 ns. . . . .	61
5	Geant4 simulations of various particles passing through 11 layers of 20 $\mu\text{m}$ thick silicon with a shortened signal length and a sampling period of 4 $\mu\text{s}$ . . . . .	61
6	Geant4 simulations of various particles passing through 11 layers of 20 $\mu\text{m}$ thick silicon with a sampling period of 4 $\mu\text{s}$ . . . . .	62
7	Geant4 simulations of various particles passing through 11 layers of 20 $\mu\text{m}$ thick silicon with shortened signal length and a sampling period of 500 ns. . . . .	62

# List of Tables

2.1	The energy resolutions of the $K_\alpha$ and $K_\beta$ -peak for both readout methods. . . . .	27
3.1	The energy resolutions extracted from the summed ToT distributions for the different detector counts. . . . .	47

# Bibliography

- [1] B. R. Martin and J. Irvine. “CERN: Past performance and future prospects: I. CERN’s position in world high-energy physics”. In: *Research Policy* 13.4 (1984), pp. 183–210. ISSN: 0048-7333. DOI: [https://doi.org/10.1016/0048-7333\(84\)90014-3](https://doi.org/10.1016/0048-7333(84)90014-3). URL: <https://www.sciencedirect.com/science/article/pii/0048733384900143>.
- [2] M. C. S. Williams. “Particle identification using time of flight”. In: *Journal of Physics G: Nuclear and Particle Physics* 39.12 (Oct. 2012), p. 123001. DOI: [10.1088/0954-3899/39/12/123001](https://doi.org/10.1088/0954-3899/39/12/123001). URL: <https://dx.doi.org/10.1088/0954-3899/39/12/123001>.
- [3] E. Nappi and J. Seguinot. “Ring Imaging Cherenkov Detectors: The state of the art and perspectives”. In: *Nuovo Cimento Rivista Serie* 28 (July 2005), pp. 1–130. DOI: [10.1393/ncr/i2006-10004-6](https://doi.org/10.1393/ncr/i2006-10004-6).
- [4] *Aerial view of the LHC accelerator complex*. CERN. 2024. URL: <https://visit.cern/node/616>.
- [5] *Discovery of the Z boson*. CERN. 2024. URL: <https://home.cern/news/news/physics/forty-years-neutral-currents>.
- [6] D. A. Glaser and D. C. Rahm. “Characteristics of Bubble Chambers”. In: *Phys. Rev.* 97 (2 Jan. 1955), pp. 474–479. DOI: [10.1103/PhysRev.97.474](https://doi.org/10.1103/PhysRev.97.474). URL: <https://link.aps.org/doi/10.1103/PhysRev.97.474>.
- [7] J. G. Wilson. *The Principles of Cloud-Chamber Technique*. CUP Archive, 1951.
- [8] G. Charpak and F. Sauli. “Multiwire proportional chambers and drift chambers”. In: *Nuclear Instruments and Methods* 162 (1979), pp. 405–428.
- [9] S. Seidel. “Silicon strip and pixel detectors for particle physics experiments”. In: *Physics Reports* 828 (2019). Silicon strip and pixel detectors for particle physics experiments, pp. 1–34. ISSN: 0370-1573. DOI: <https://doi.org/10.1016/j.physrep.2019.09.003>. URL: <https://www.sciencedirect.com/science/article/pii/S0370157319302923>.
- [10] F. Hartmann. “Silicon tracking detectors in high-energy physics”. In: *Nuclear Instruments and Methods in Physics Research Section A: Accelerators, Spectrometers, Detectors and Associated Equipment* 666 (2012). Advanced Instrumentation, pp. 25–46. ISSN: 0168-9002. DOI: <https://doi.org/10.1016/j.nima.2011.11.005>. URL: <https://www.sciencedirect.com/science/article/pii/S0168900211020389>.

## Bibliography

- [11] M. Turala. “Silicon tracking detectors—historical overview”. In: *Nuclear Instruments and Methods in Physics Research Section A: Accelerators, Spectrometers, Detectors and Associated Equipment* 541.1 (2005). Development and Application of Semiconductor Tracking Detectors, pp. 1–14. ISSN: 0168-9002. DOI: <https://doi.org/10.1016/j.nima.2005.01.032>. URL: <https://www.sciencedirect.com/science/article/pii/S0168900205000446>.
- [12] The ALICE Collaboration et al. “The ALICE experiment at the CERN LHC”. In: *Journal of Instrumentation* 3.08 (Aug. 2008), S08002. DOI: 10.1088/1748-0221/3/08/S08002. URL: <https://dx.doi.org/10.1088/1748-0221/3/08/S08002>.
- [13] The ALICE collaboration. *The ALICE experiment: a journey through QCD*. Nov. 2022. DOI: 10.48550/arXiv.2211.04384.
- [14] P. Braun-Munzinger and J. Stachel. “The quest for the quark-gluon plasma”. In: *Nature* 448.7151 (July 2007), pp. 302–309. ISSN: 1476-4687. DOI: 10.1038/nature06080. URL: <https://doi.org/10.1038/nature06080>.
- [15] G. Contin. “The MAPS-based ITS Upgrade for ALICE”. In: Feb. 2020, p. 003. DOI: 10.22323/1.373.0003.
- [16] ALICE TPC collaboration and others. “The upgrade of the ALICE TPC with GEMs and continuous readout”. In: *Journal of Instrumentation* 16.03 (Mar. 2021), P03022. DOI: 10.1088/1748-0221/16/03/P03022. URL: <https://dx.doi.org/10.1088/1748-0221/16/03/P03022>.
- [17] F. Sauli. “GEM: A new concept for electron amplification in gas detectors”. In: *Nuclear Instruments and Methods in Physics Research Section A: Accelerators, Spectrometers, Detectors and Associated Equipment* 386.2 (1997), pp. 531–534. ISSN: 0168-9002. DOI: [https://doi.org/10.1016/S0168-9002\(96\)01172-2](https://doi.org/10.1016/S0168-9002(96)01172-2). URL: <https://www.sciencedirect.com/science/article/pii/S0168900296011722>.
- [18] R. Turchetta, J. Berst, B. Casadei, G. Claus, C. Colledani, W. Dulinski, Y. Hu, D. Husson, J. Le Normand, J. Riester, G. Deptuch, U. Goerlach, S. Higuieret, and M. Winter. “A monolithic active pixel sensor for charged particle tracking and imaging using standard VLSI CMOS technology”. In: *Nuclear Instruments and Methods in Physics Research Section A: Accelerators, Spectrometers, Detectors and Associated Equipment* 458.3 (2001), pp. 677–689. ISSN: 0168-9002. DOI: [https://doi.org/10.1016/S0168-9002\(00\)00893-7](https://doi.org/10.1016/S0168-9002(00)00893-7). URL: <https://www.sciencedirect.com/science/article/pii/S0168900200008937>.
- [19] L. Greiner. “MAPS application in the STAR and ALICE Experiments”. In: *Nuclear Instruments and Methods in Physics Research Section A: Accelerators, Spectrometers, Detectors and Associated Equipment* 942 (2019), p. 162283. ISSN: 0168-9002. DOI: <https://doi.org/10.1016/j.nima.2019.06>.

## Bibliography

024. URL: <https://www.sciencedirect.com/science/article/pii/S0168900219308642>.
- [20] *Technical Design Report for the Upgrade of the ALICE Inner Tracking System*. Tech. rep. 2014. DOI: 10.1088/0954-3899/41/8/087002. URL: <http://cds.cern.ch/record/1625842>.
- [21] M. Mager. “ALPIDE, the Monolithic Active Pixel Sensor for the ALICE ITS upgrade”. In: *Nuclear Instruments and Methods in Physics Research Section A: Accelerators, Spectrometers, Detectors and Associated Equipment* 824 (2016). Frontier Detectors for Frontier Physics: Proceedings of the 13th Pisa Meeting on Advanced Detectors, pp. 434–438. ISSN: 0168-9002. DOI: <https://doi.org/10.1016/j.nima.2015.09.057>. URL: <https://www.sciencedirect.com/science/article/pii/S0168900215011122>.
- [22] G. Aglieri Rinella. “The ALPIDE pixel sensor chip for the upgrade of the ALICE Inner Tracking System”. In: *Nuclear Instruments and Methods in Physics Research Section A: Accelerators, Spectrometers, Detectors and Associated Equipment* 845 (2017). Proceedings of the Vienna Conference on Instrumentation 2016, pp. 583–587. ISSN: 0168-9002. DOI: <https://doi.org/10.1016/j.nima.2016.05.016>. URL: <https://www.sciencedirect.com/science/article/pii/S0168900216303825>.
- [23] L. Musa. *Letter of Intent for an ALICE ITS Upgrade in LS3*. Tech. rep. Geneva: CERN, 2019. DOI: 10.17181/CERN-LHCC-2019-018. URL: <http://cds.cern.ch/record/2703140>.
- [24] L. Aglietta. “ALICE silicon tracker upgrades for LHC Run 4 and beyond”. In: *Nuclear Instruments and Methods in Physics Research Section A: Accelerators, Spectrometers, Detectors and Associated Equipment* 1069 (2024), p. 169812. ISSN: 0168-9002. DOI: <https://doi.org/10.1016/j.nima.2024.169812>. URL: <https://www.sciencedirect.com/science/article/pii/S0168900224007381>.
- [25] G. Aglieri Rinella et al. “Characterization of analogue Monolithic Active Pixel Sensor test structures implemented in a 65 nm CMOS imaging process”. In: *Nuclear Instruments and Methods in Physics Research Section A: Accelerators, Spectrometers, Detectors and Associated Equipment* 1069 (2024), p. 169896. ISSN: 0168-9002. DOI: <https://doi.org/10.1016/j.nima.2024.169896>. URL: <https://www.sciencedirect.com/science/article/pii/S0168900224008222>.
- [26] M. Šuljić et al. “Digital Pixel Test Structures implemented in a 65 nm CMOS process”. In: *Nucl. Instrum. Methods Phys. Res., A* 1056 (2023), p. 168589. DOI: 10.1016/j.nima.2023.168589. arXiv: 2212.08621. URL: <http://cds.cern.ch/record/2845385>.

## Bibliography

- [27] S. Bugiel et al. "Charge sensing properties of monolithic CMOS pixel sensors fabricated in a 65nm technology". In: *Nuclear Instruments and Methods in Physics Research Section A: Accelerators, Spectrometers, Detectors and Associated Equipment* 1040 (2022), p. 167213. ISSN: 0168-9002. DOI: <https://doi.org/10.1016/j.nima.2022.167213>. URL: <https://www.sciencedirect.com/science/article/pii/S016890022200568X>.
- [28] P. V. Leitao et al. In: 18.01 (Jan. 2023), p. C01044. DOI: 10.1088/1748-0221/18/01/C01044. URL: <https://dx.doi.org/10.1088/1748-0221/18/01/C01044>.
- [29] G. H. Hong. "Monolithic Stitched Sensor (MOSS) Development for the ALICE ITS3 Upgrade". In: *PoS Pixel2022* (2023), p. 028. DOI: 10.22323/1.420.0028. URL: <https://cds.cern.ch/record/2870190>.
- [30] L. Cecconi et al. "Design and readout architecture of a monolithic binary active pixel sensor in TPSCo 65nm CMOS imaging technology". In: *Journal of Instrumentation* 18.02 (Feb. 2023), p. C02025. DOI: 10.1088/1748-0221/18/02/C02025. URL: <https://dx.doi.org/10.1088/1748-0221/18/02/C02025>.
- [31] Pico Technology. *PicoScope 6000E Series Brochure*. Accessed: 2024-10-10. 2024. URL: <https://www.priggen.com/ddownloads/PicoScope%206000E%20Serie%20Broschuere.pdf>.
- [32] U. Farooq, Z. Marrakchi, and H. Mehrez. "FPGA Architectures: An Overview". In: *Tree-based Heterogeneous FPGA Architectures: Application Specific Exploration and Optimization*. New York, NY: Springer New York, 2012, pp. 7–48. ISBN: 978-1-4614-3594-5. DOI: 10.1007/978-1-4614-3594-5\_2. URL: [https://doi.org/10.1007/978-1-4614-3594-5\\_2](https://doi.org/10.1007/978-1-4614-3594-5_2).
- [33] M. Böhmer, G. Korcyl, L. Maier, J. Michel, A. Neiser, M. Palka, M. Penschuck, P. Strzempek, M. Traxler, and C. Ugur. *A Users Guide to the TRB3 and FPGA-TDC Based Platforms*. July 2024. URL: <http://jspc29.x-matter.uni-frankfurt.de/docu/trb3docu.pdf>.
- [34] J. Kalisz. "Review of methods for time interval measurements with picosecond resolution". In: *Metrologia* 41.1 (Dec. 2003), p. 17. DOI: 10.1088/0026-1394/41/1/004. URL: <https://dx.doi.org/10.1088/0026-1394/41/1/004>.
- [35] J. Adamczewski-Musch, S. Linev, and C. Ugur. *Online Calibration of the TRB3 FPGA TDC with DABC Software*. The TRB3 collaboration. Poster presented at the 20th IEEE Real-Time Conference, 5–10 June 2016, Padova, Italy. 2016. URL: [http://jspc29.x-matter.uni-frankfurt.de/trb3/publications/RT2016\\_Poster\\_trbtcd\\_2.pdf](http://jspc29.x-matter.uni-frankfurt.de/trb3/publications/RT2016_Poster_trbtcd_2.pdf).

## Bibliography

- [36] A. S. Triolo. “Calibration and Performance of the Upgraded ALICE Inner Tracking System”. In: *arXiv preprint arXiv:2409.19810* (2024). Prepared for submission to JINST, 25th International Workshop on Radiation Imaging Detectors, 30th June - 04th July 2024, Lisbon, Portugal. URL: <https://arxiv.org/abs/2409.19810>.
- [37] A. Sofia Triolo. personal communication. July 23, 2024.
- [38] J. Bernhard et al., eds. *CERN Proton Synchrotron East Area Facility: Upgrades and renovation during Long Shutdown 2*. CERN Yellow Reports: Monographs CERN-2021-004. Accepted in Oct. 2021 by the CERN Reports Editorial Board. Geneva: CERN, 2021. DOI: 10.23731/CYRM-2021-004. URL: <https://doi.org/10.23731/CYRM-2021-004>.
- [39] The ALICE collaboration. *Technical Design report for the ALICE Inner Tracking System 3 - ITS3 ; A bent wafer-scale monolithic pixel detector*. Tech. rep. Co-project Manager: Magnus Mager, [magnus.mager@cern.ch](mailto:magnus.mager@cern.ch). Geneva: CERN, 2024. URL: <https://cds.cern.ch/record/2890181>.
- [40] W. Leo. *Techniques for Nuclear and Particle Physics Experiments: A How-to Approach*. 2nd. Berlin, Heidelberg: Springer, 1994. ISBN: 978-3-642-57920-2. DOI: 10.1007/978-3-642-57920-2.
- [41] ALICE Collaboration. *Performance plots of ITS2 PID capabilities with Machine Learning*. Accessed: 2024-10-06. 2024. URL: <https://alice-figure.web.cern.ch/node/29801>.
- [42] ALICE Collaboration. “ALICE 3: A Proposal for a Next Generation Heavy Ion Detector”. In: LHCC-I-038 (2022). CERN-LHCC-2022-009, arXiv:2211.02491v1 [physics.ins-det]. URL: <https://arxiv.org/abs/2211.02491>.
- [43] X. Ai, C. Allaire, N. Calace, A. Czirkos, M. Elsing, I. Ene, R. Farkas, L.-G. Gagnon, R. Garg, P. Gessinger, H. Grasland, H. M. Gray, C. Gumpert, J. Hrdinka, B. Huth, M. Kiehn, F. Klimpel, B. Kolbinger, A. Krasznahorkay, R. Langenberg, C. Leggett, G. Mania, E. Moyse, J. Niermann, J. D. Osborn, D. Rousseau, A. Salzburger, B. Schlag, L. Tompkins, T. Yamazaki, B. Yeo, and J. Zhang. “A Common Tracking Software Project”. In: *Computing and Software for Big Science* 6.1 (Apr. 2022), p. 8. ISSN: 2510-2044. DOI: 10.1007/s41781-021-00078-8. URL: <https://doi.org/10.1007/s41781-021-00078-8>.
- [44] S. Agostinelli, J. Allison, K. Amako, et al. “Geant4 — a simulation toolkit”. In: *Nuclear Instruments and Methods in Physics Research Section A: Accelerators, Spectrometers, Detectors and Associated Equipment* 506.3 (2003), pp. 250–303. ISSN: 0168-9002. DOI: [https://doi.org/10.1016/S0168-9002\(03\)01368-8](https://doi.org/10.1016/S0168-9002(03)01368-8). URL: <https://www.sciencedirect.com/science/article/pii/S0168900203013688>.